Journal of Carbon Research

MDPI

Article

Moderate-Temperature Carbon Capture Using Thermally Pre-Treated Dolomite: A Novel Approach

Iyiade G. Alalade, Javier E. Morales-Mendoza, Alma B. Jasso-Salcedo, Jorge L. Domínguez-Arvizu, Blanca C. Hernández-Majalca, Hammed A. Salami, José L. Bueno-Escobedo, Luz I. Ibarra-Rodriguez, Alejandro López-Ortiz * and Virginia H. Collins-Martínez

Departamento de Ingeniería y Química de Materiales, Centro de Investigación en Materiales Avanzados S.C., Miguel de Cervantes 120, Chihuahua 31136, Mexico; iyiade.alalade@cimav.edu.mx (I.G.A.); javier.morales@cimav.edu.mx (J.E.M.-M.); alma.jasso@cimav.edu.mx (A.B.J.-S.); jorge.dominguez@cimav.edu.mx (J.L.D.-A.); blanca.hernandez@cimav.edu.mx (B.C.H.-M.); hammed.adeniyi@cimav.edu.mx (H.A.S.); jose.bueno@cimav.edu.mx (J.L.B.-E.); luz.ibarra@cimav.edu.mx (L.I.I.-R.); virginia.collins@cimav.edu.mx (V.H.C.-M.)

* Correspondence: alejandro.lopez@cimav.edu.mx

Abstract: This study investigates a novel approach to moderate-temperature carbon capture by examining the enhanced performance of thermally pre-treated dolomite. To obtain mixed oxides, dolomite samples were prepared via calcination in a quartz cylindrical furnace under an ambient atmosphere at 900 °C, and subsequently thermally pre-treated under an inert (argon) stream at 650 °C. Characterization of the as-prepared samples involved morphological, structural, textural, and optical features examined through XRD, BET, SEM-EDS, FT-IR, and RAMAN, XPS, and UV-vis spectroscopy, whereas TGA and subsequent multicyclic tests were used to study the CO_2 sorption. The dolomite sample calcined at 900 °C for 60 min, and after being activated under an inert atmosphere (argon), labeled PCD60Act, exhibited the highest CO_2 uptake of 0.477 $g_{CO2}/g_{sorbent}$; after 15 sorption–regeneration cycles, it still retained a CO_2 uptake of 0.38 $g_{CO2}/g_{sorbent}$ at 650 °C, and it was also successfully regenerated at this moderate temperature, demonstrating 84% capture capacity retention. These remarkable results are explained by the crystalline defects generated during the thermal pre-treatments of the dolomite. This research offers valuable perspectives on the viability of employing thermally pre-treated dolomite as an inexpensive, thermally stable, and moderate-temperature regenerable CaO-based sorbent for applications in CO_2 removal in the context of integrated carbon capture and conversion (ICCC) for the production of high-purity hydrogen.

Keywords: thermal pre-treatment; dolomite; CaO-based sorbent; hydrogen; CO_2 capture; ICCC

check for updates

Academic Editor: Jian Sun

Received: 29 April 2025
Revised: 23 May 2025
Accepted: 28 May 2025
Published: 5 June 2025

Citation: Alalade, I.G.; Morales-Mendoza, J.E.; Jasso-Salcedo, A.B.; Domínguez-Arvizu, J.L.; Hernández-Majalca, B.C.; Salami, H.A.; Bueno-Escobedo, J.L.; Ibarra-Rodriguez, L.I.; López-Ortiz, A.; Collins-Martínez, V.H. Moderate-Temperature Carbon Capture Using Thermally Pre-Treated Dolomite: A Novel Approach. *C* **2025**, *11*, 37. https://doi.org/10.3390/c11020037

Copyright: © 2025 by the authors. Licensee MDPI, Basel, Switzerland. This article is an open access article distributed under the terms and conditions of the Creative Commons Attribution (CC BY) license (https://creativecommons.org/licenses/by/4.0/).

1. Introduction

Since the mid-20th century, anthropogenic CO_2 emissions have raised global concerns, with amine-based chemical absorption dominating industrial capture methods, despite drawbacks such as high energy demands, corrosion, poor solvent regeneration, and environmental issues [1]. As alternatives, solid sorbents in carbon capture and utilization (CCU) technologies have gained attention due to their lower energy requirements [2,3]. Among those, CaO-based sorbents are promising for their high theoretical CO_2 capacity (~0.78 $g_{CO2}/g_{sorbent}$), fast sorption kinetics, abundance, low cost, and operability at flue gas temperatures (>500 °C) [4–6], positioning them as viable solutions to emission challenges [7].

However, CaO-based sorbents suffer from fast performance degradation due to sintering during repeated high-temperature (>800 °C) cycles [8–11], driven by the low Tammann temperature (~529 °C) of $CaCO_3$ [12]. Sintering causes pore blockage and inhibits CO_2 diffusion due to surface $CaCO_3$ buildup [13].

To mitigate this, several strategies have been explored, such as inert additives [14–16], organic acid treatments [17,18], hydration reactivation [19,20], thermal pre-treatment [21], sintering-resistant precursors [22,23], and alkali-molten-salt promoters [24–26]. Notably, combining CaO with inert supports and modifying precursors with salts like $NaNO_3$ enhances sorbent performance by promoting CO_2 diffusion, while Al-based supports such as $Ca_{12}Al_{14}O_{33}$, Al_2O_3, and $Ca_9Al_6O_{18}$ have shown promising results [27–34]. Also, MgO has also emerged as an effective support due to its high Tammann temperature (1276 °C), acting as a structural stabilizer in CaO–MgO systems [25,35–39]. Furthermore, thermal pre-treatment of calcite yields CaO-based sorbents with increased oxygen vacancies and crystalline defects, thus improving sorption–regeneration kinetics [40–43].

Despite these advances, gaps remain. The influence of MgO on calcined dolomite sorbent stability at moderate sorption and regeneration temperatures (≤650 °C) has not been explored [36,37]. Most studies emphasize high-temperature calcination and sorption (>700 °C), neglecting energy-saving alternatives [27–31]. Additionally, conflicting results regarding porosity and structural crystalline defects (i.e., oxygen vacancies, crystallite size, etc.) suggest unresolved challenges in sorbent design [38,44–51].

Therefore, this study addresses these gaps by developing a simple, cost-effective approach to prepare and optimize a dolomite-based sorbent prepared from air-calcined natural dolomite and further modified by an inert-atmosphere thermal pre-treatment. The work focuses on establishing the relationship between microstructural defects (e.g., oxygen vacancies, pore volume, crystallite size, etc.) and MgO fixed content on calcined dolomite thermal stabilization and enhanced CO_2 sorption performance at moderate temperatures (≤650 °C). Additionally, it targets dolomite regeneration at temperatures lower than those typically required for CaO-based sorbents (>700 °C), improving energy efficiency. The goal is to design a dolomite-based sorbent compatible with dual-function materials (DFMs) for integrated carbon capture and conversion (ICCU) technologies, particularly emerging hydrogen processes, like dry reforming of methane (DRM), which demand cost-effective sorbents with high thermal stability under low regeneration temperatures. Our approach builds on prior work by Hu et al. [36] and Li et al. [37], but diverges in its focus on natural dolomite precursors and lower-temperature optimization. To our knowledge, this represents the first demonstration of dolomite-based sorbent regeneration at $T < 700$ °C.

2. Materials and Methods

2.1. Sorbent Preparation

The naturally occurring dolomite ($CaMg(CO_3)_2$) used in this investigation was procured from Vitromex®, Monterrey, Mexico, (a subsidiary of Mohawk® Industries Inc.). Calcination of dolomite at 900 °C in a quartz cylindrical furnace, at a temperature ramp of 10 °C/min, [52,53] in an open-air atmosphere, was performed first to compare the CO_2 sorption performance of dolomite calcined for different calcination times (30, 60, 120, and 240 min), labeled PCD30, PCD60, PCD120, and PCD240, respectively. These samples were evaluated at a moderate temperature for one CO_2 sorption cycle at 450 °C, for 2 h and 90% CO_2/Ar. Additionally, reagent-grade calcium carbonate ($CaCO_3$, Acros® procured from Merck, Mexico, 98.5%) was employed as a reference material, underwent the same heat treatment as previous PCD samples, and was labeled pristine CaO, while a fresh dolomite sample was prepared via TGA under an air atmosphere at 900 °C, and labeled UD.

2.1.1. Sorbent Activation

In a second study, the effect of thermal pre-treatment (activation) on the material properties, as well as on the CO_2 capture performance, of all PCD samples was examined. This consisted of exposing the calcined dolomite to an inert atmosphere (Argon, AOC Gases, Chihuahua, México) for 30 min at 650 °C to promote crystalline defects. Upon this activation, the PCD samples were labeled PCD30Act, PCD60Act, PCD120Act, and PCD240Act. Thereafter, these samples obtained were desiccator-stored to consider the hygroscopicity of the mixed oxides (CaO–MgO) [54,55]. Sorption evaluations began by changing the gas feed from argon to CO_2 at the target sorption temperatures (300–800 °C) for 60 min, unless otherwise specified, with sample masses recorded every second by the data acquisition system of a thermogravimetric analyzer (TA Instruments® TGA-Q500, Waters Corporation®, Mexico City, Mexico). Resulting from this evaluation, the best sorbent was selected from among all the activated PCD samples, based on CO_2 sorption performance, capacity, favorable kinetics, and optimal sorption temperature.

2.1.2. CO_2 Concentration Effect and Multicycle Tests

The effect of CO_2 concentration was evaluated for the best activated PCD sample. This involved exposing it to 90, 80, and 70% CO_2/Ar atmospheres to find the optimal CO_2 concentration based on the highest CO_2 capture capacity and kinetics. Moreover, the stability of the best activated PCD sample was evaluated through multicycle sorption–regeneration schemes via a thermogravimetric analyzer (TA Instruments TGA-Q500) at atmospheric pressure. The reaction gas flow rate was maintained at 100 mL/min, calibrated with a mass flow controller. The reactor tube and sample pan had diameters of 38 mm and 24 mm, respectively. For each sorption–regeneration test, 20 mg of sample was evenly distributed in the sample holder to minimize resistance to CO_2 diffusion through the powder bed—an effect known to become significant with sample masses greater than approximately 40 mg [56].

Multicyclic (15) tests were performed at 450 °C (isothermal for 30 min, 90% CO_2 atmosphere) and 650 °C (isothermal for 15 min, argon atmosphere) for a sorption–regeneration cycle, respectively, using temperature-swing sorption (TSS). Also, 15 cyclic sorption–regeneration tests were performed at 650 °C isothermally, where the sorption (90% CO_2 atmosphere) and regeneration (argon atmosphere) cycles lasted for 10 and 40 min, respectively. The increase in sample weight indicated sorption (carbonation), while the decrease indicated regeneration (decarbonation). The CO_2 uptake capacity in weight percent was determined by dividing the mass gained during sorption by the sorbents' mass following activation, as shown in Equation (1) [48].

$$CO_2 \text{ uptake capacity} = M_f - M_i / M_i \times 100\% \quad (1)$$

where M_f is the sorbent mass after sorption and M_i is the initial sorbent mass after activation.

2.1.3. CO_2 Sorption Repeatability Analysis

The best-performing activated PCD sample was analyzed for repeatability with CO_2 sorption performed in triplicate, and the data are presented as the mean ± standard deviation (SD). Y-error bars in all graphs represent the standard deviation of three independent measurements for each sample. Statistical analysis was carried out using OriginPro, and standard deviations were computed based on the spread of replicate data points.

2.2. Characterization Methods

2.2.1. Inductively Coupled Plasma Optical Emission Spectroscopy

Elemental composition evaluation of the fresh dolomite sample was conducted using inductively coupled plasma optical emission spectroscopy (ICP-OES) (Thermo Scientific® iCAP 6000 SERIES, Waltham, MA, USA). The instrument featured a high-resolution echelle-type polychromator and charge injection device detectors, accompanied by iTEVA software (version 2.0) for simultaneous multi-element detection. The sample was prepared via wet digestion of 2 mg of the dolomite sample with 4 mL of aqua regia (V_{HCl}:V_{HNO3} = 3:1).

2.2.2. Scanning Electron Microscopy

The morphologies of the prepared dolomite samples were analyzed using a field-emission scanning electron microscope (FESEM, JEOL JSM-5800LV, Tokyo, Japan) equipped with energy-dispersive spectroscopy (EDS) at an accelerating voltage of 20 kV. Particle size distributions were measured by image analysis (ImageJ software®, Version 1.54, National Institutes of Health (NIH), Bethesda, MD, USA) using the SEM micrographs.

2.2.3. Surface Area and Porosity Analyses

Nitrogen (N_2) adsorption–desorption isotherms of the samples investigated were estimated at 77.35 K (−196 °C) using a physical adsorption analyzer (3P Micro Series, 3P Instruments, Odelzhausen Germany). Before the evaluation, the samples were purged at 250 °C for 3 h [57]. The specific surface areas (S_{BET}), pore volumes, and average pore diameters of the samples were determined using the Brunauer–Emmett–Teller (BET) and Barrett–Joyner–Halenda (BJH) models.

2.2.4. Powder X-Ray Diffraction

Phase distributions of the prepared samples were determined by powder X-ray diffractometry (PANalytical X'Pert Pro, Malvern Panalytical, Westborough, MA, USA and equipped with Cu Kα radiation λ = 1.54178 Å). Also, in situ XRD measurement was performed on the fresh dolomite sample from room temperature to 900 °C at a 10 °C/min heating ramp, while in an air atmosphere and at atmospheric pressure, to study the decomposition of the dolomite precursor into its mixed oxides (CaO–MgO). X-ray reflections were obtained in the 2θ range from 10° to 90°, with 0.05° per step, at 45 kV and 40 mA for 30 min. Rietveld refinement was performed using the FullProf® Version 4.1, program, fitting the diffraction peaks with a Thompson–Cox–Hastings-type function in order to determine the percentage of the crystallographic phases present in the materials (e.g., CaO, MgO, etc.), the crystallite size (D) through peak broadening analysis, and the strain generated in the crystal lattice. For each refinement, both the goodness-of-fit value (χ^2) and the crystallographic parameters obtained from each analysis using this method are included.

The crystallite size (D) of the individual phases obtained were estimated according to Scherrer's equation (Equation (2)) [50], using the most intense peak reflection for every phase.

$$D = k\lambda/\beta\cos\theta \quad (2)$$

where D represents the crystallite size (nm), β denotes the peak breadth of half height in the XRD spectra, λ signifies the X-ray wavelength (0.15406 nm), θ refers to the Bragg angle in degrees, and k is the Scherrer constant.

2.2.5. Fourier-Transform Infra-Red Spectroscopy

A Perkin Elmer (ATR) Frontier FT-IR spectrometer was used in this study, and the sorbent samples were evaluated in KBr media [58]. The spectral profiles were recorded

within the range of 4000–500 cm^{-1}, and the intensities of the bands were expressed in transmittance (a.u).

2.2.6. Raman Spectroscopy

The Raman spectra for the prepared samples were obtained via an XploRA INV-Horiba® (Kyoto, Japan) inverted Raman microscope, in the 20–2000 cm^{-1} range, equipped with a power of 50 mW and a 532 nm laser for excitation.

2.2.7. X-Ray Photoelectron Spectroscopy

The XPS analyses were performed on a Thermo Fisher Scientific Escalab 250Xi, Massachusetts, USA, maintaining a base analysis vacuum pressure of ~10^{-8} mbar [38]. The excitation of the analyzed photoelectrons was accomplished with a monochromatic Al Kα X-ray source (1486.68 eV) with a 45° take-off angle and an analysis radius (size of the X-ray spot) of 650 µm. The analysis conditions for the low-resolution survey spectrum were a 1 eV step size with a step energy of 150 eV, while a step energy of 20 eV was used at 0.1 eV/step for the enhanced-resolution areas.

2.2.8. Ultraviolet-Visible Spectroscopy

The optical absorbance spectra of the samples were recorded from 200 to 800 nm using a UV-visible NIR spectrophotometer (Cary 5000 model). The direct band gaps (eV) of the as-prepared samples were extrapolated using the Tauc–Wood relation and Kubelka–Munk function F (R), as shown in Equation (3).

$$F(R) = (1 - R)^2/2R \quad (3)$$

where R is the diffuse reflectance of the sample.

3. Results and Discussion

3.1. Inductively Coupled Plasma Optical Emission Spectroscopy Results

The theoretical composition of dolomite, by weight, includes 30.4% CaO, 21.8% MgO, and 47.8% CO_2 [59,60]. It is conventionally represented using the chemical expression $CaMg(CO_3)_2$, reflecting a 1:1 ratio of calcium (Ca) to magnesium (Mg). However, in nature, numerous compositional variations can be found in which the ratio of Mg to Ca is very different. Table S1 shows the elemental composition of the fresh dolomite sample ($d_p \approx 180$ µm) used in this investigation, as analyzed by inductively coupled plasma optical emission spectroscopy (ICP-OES). Since the dolomite sample presented a total carbon content of 12.5 wt.%, further theoretical calculation indicated that the ratio between Ca and Mg was 1.2:1, thus making it a calcium-rich dolomite. The disparity between the calculated composition and the reported stoichiometric ratio can be attributed to the mineral source of the dolomite.

3.2. Scanning Electron Microscopy Results

The SEM micrograph in Figure 1a depicts the surface morphology of the fresh dolomite, which appears to be composed of interlocking crystals, each exhibiting distinct faces and edges in comparison with the micrographs of PCD240 and PCD60 (Figure 1b,c), portraying the evolution of pore networks after modification via heat treatment. The particles for both PCD240 and PCD60 exhibit irregular shapes with sharp edges and fractured surfaces, indicative of thermal decomposition. The release of CO_2 during calcination created a porous structure, with visible voids and microcracks throughout the material, with some areas of PCD240 (Figure 1b) possibly showing sintering effects, where smaller particles start to agglomerate due to the long calcination time. Conversely, PCD60 (Figure 1c) demonstrates

a rough and granular surface displaying a complex, fractal-like morphology that reflects the breakdown of the original carbonate particles. Previous studies have observed comparable morphological structures [61], where these features were attributed to pore formation due to CO_2 evolution. EDS spectra (Figure 1f,g) confirm the complete decomposition of dolomite into mixed oxides (CaO–MgO).

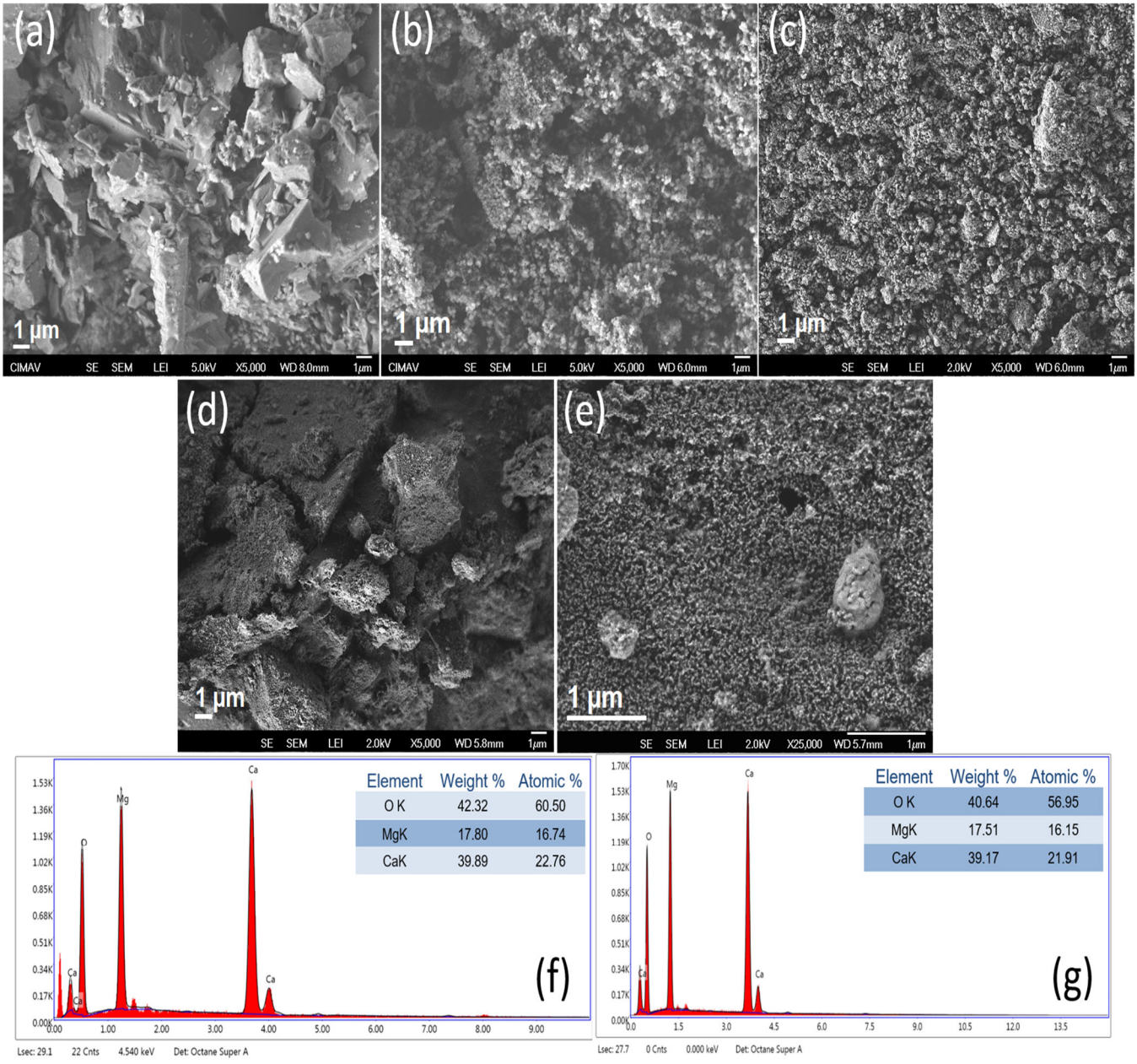


Figure 1. SEM micrographs of (**a**) fresh dolomite, (**b**) PCD240, (**c**) PCD60, (**d**) PCD60Act after 15 sorption–regeneration cycles ×5000, and (**e**) PCD60Act after 15 sorption–regeneration cycles ×25,000. (**f**) EDS of PCD240 and (**g**) EDS of PCD60.

Figure S1a,b illustrate the particle size distributions of the calcined dolomite samples (PCD240 and PCD60). The obtained mean distributions of PCD240 and PCD60 were 13.4 µm and 198 nm, respectively, with the histograms indicating moderately unimodal distributions. However, the extended calcination time for PCD240 resulted in an enlarged average particle size, mainly attributed to sintering.

3.3. Thermal Decomposition of Dolomite

3.3.1. Thermogravimetric Analysis Results

To study the thermal behavior of dolomite, its thermal decomposition into its constituent oxides (CaO–MgO) is presented in Figure S2. The TGA revealed that the maximum weight loss occurred at approximately 760 °C, indicating a 53.3 wt.% loss on fusion, which exceeds the reference theoretical mass loss for stoichiometric dolomite (47.8 wt.%) by 5.5 wt.%. This deviation in weight loss confirms the presence of trace impurities in the dolomite sample. These dolomite decomposition results are consistent with studies suggesting that dolomite decomposes in air via a one-step pathway [62,63].

3.3.2. Powder X-Ray Diffraction Results

The in situ XRD patterns illustrating the heat treatment of dolomite from room temperature to 900 °C, under an ambient atmosphere, to yield its corresponding oxides (CaO–MgO) are presented in Figure 2a,b. The diffractogram in Figure 2a exhibits the characteristic diffraction peaks of dolomite (D) rich in calcite (C) from room temperature up to 700 °C. As the temperature rises to 800 °C, these peaks completely disappear (Figure 2b), while peaks corresponding to CaO (ICDD 82-1690) and MgO (ICDD 87-0652) emerge, indicating that a single calcination step at 900 °C is sufficient to produce the constituent oxides of dolomite (CaO–MgO), confirming the EDS spectra and TGA findings in Figure 1f,g and Figure S2, respectively. Also, peaks from the platinum sample holder (Pt) are present in the patterns collected.

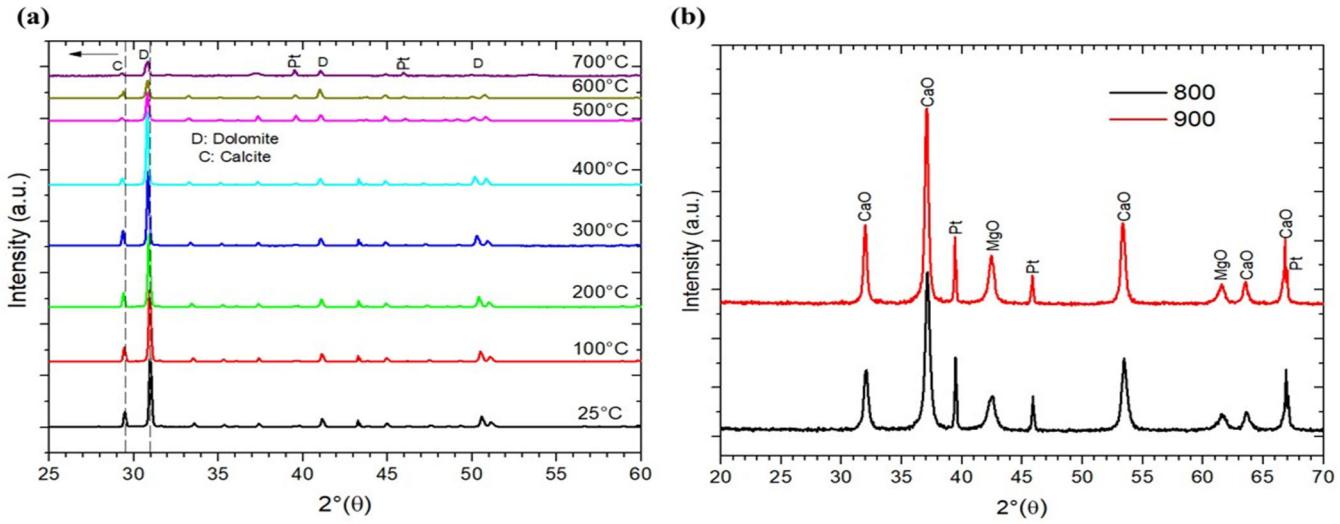


Figure 2. In situ XRD patterns of dolomite during calcination from room temperature up to (**a**) 700 °C and (**b**) 900 °C. In panel (**a**), the arrow indicates that increasing the calcination temperature causes a shift in the main reflections of dolomite and calcite toward lower 2θ angles.

Therefore, the process of thermal decomposition for dolomite can be outlined as follows:

$$CaMg(CO_3)_{2(s)} \rightarrow CaO{\cdot}MgO_{(s)} + 2CO_{2(g)} \quad (4)$$

3.4. Surface Area and Porosity Analyses Results

Table 1 shows the textural properties of the calcined dolomite sorbents (PCD240 and PCD60), as well as the crystallite sizes of CaO and MgO derived using the Scherrer equation. The values acquired for pristine CaO are also presented for comparison purposes. The results show evidence that 60 min dolomite calcination at 900 °C yielded superior textural properties compared to the dolomite calcined for 240 min, as expected. PCD60 (26 m^2/g)

generated as much as 5 times the surface area of PCD240 (5 m^2/g), and almost 2 times that of pristine CaO (16 m^2/g). Also, the crystallite sizes achieved for CaO (41 nm) and MgO (25 nm) in PCD60 were smaller than those in PCD240, of 50 and 29 nm, respectively. This supports the fact that long calcination periods can be detrimental to the textural properties of a dolomite sorbent [64,65].

Table 1. Textural properties of fresh and as-prepared calcined CaO-based sorbents.

Sorbent	S_{BET} (m^2/g)	Pore Volume (cm^3/g)	Pore Size (nm)	Crystallite Size (nm)	
				CaO	MgO
Fresh dolomite	0.6	0.002	13	-	-
PCD240	5	0.01	8	50	29
PCD60	26	0.06	9	41	25
Pristine CaO	16	0.02	6.6	47	-

The pore size distributions and N_2 adsorption–desorption isotherm curves of PCD240 and PCD60 are presented in Figure S3 and Figure S4, respectively, revealing that the calcined dolomite sorbents are mainly mesoporous, with pore sizes within the 2–10 nm range. According to Figure S4, PCD240 and PCD60 presented type III isotherms and H3 hysteresis loops. This implies that CO_2 sorption tended to cluster around the most favorable sites on the surface of the PCD sorbents, according to the 2015 IUPAC classification [66]. Despite PCD240 and PCD60 having similar pore size distributions, the synergy between the mesoporosity and higher surface area of PCD60 is desirable. This combination presumably enhances gas diffusion and accessibility, while aiding the significant volume change between CaO (16.7 $cm^3 \cdot mol^{-1}$) and $CaCO_3$ (36.9 $cm^3 \cdot mol^{-1}$) during the conversion process, thereby preserving the pore structure [67].

Furthermore, the crystallite size, which is a key structural property, can be used to estimate the dislocation density (ρ) in the sample. Dislocation density (ρ), a measure of the number of imperfections in a sample, is described as the aggregate length of dislocation lines per unit volume of a crystal [68], as indicated in Equation (5) using the inverse square of the crystallite size [69–71] calculated by Scherrer's equation (Equation (2)). This equation provides an estimation of the number of defects present within a sample.

$$\rho = 1/D^2 \quad (5)$$

where D denotes the crystallite size and ρ refers to the dislocation density.

The estimated specific quantity of defects per gram of sorbent is provided in Table 2. Hence, the estimated dislocation density of CaO in calcined dolomite is shown to be dependent on the crystallite sizes, as presented in Table 1. The observed elevated estimate for the dislocation density for PCD60 is linked to the small CaO crystallites generated in the sorbent on calcination during the dolomite sample preparation.

Table 2. Estimated dislocation density after calcination of selected CaO-based sorbents.

Sorbent	Dislocation Density (10^{10} m^{-2})
	CaO
PCD60	60
PCD240	40
Pristine CaO	45

3.5. The Effect of Time on the Calcination of Dolomite

Figure 3 shows the CO_2 sorption profile of PCD 30, 60, 120, and 240. The graph depicts no apparent difference in CO_2 uptake, as all PCD samples achieved almost the same CO_2 sorption performance (0.34 $g_{CO2}/g_{sorbent}$) after 2 h of sorption at 450 °C. The calcination conditions have been identified as crucial during the preparation of a sorbent [53]. These conditions are connected to developing an adequate surface area, pore volume, and carbon residue, thereby modifying the sorbent's uptake performance.

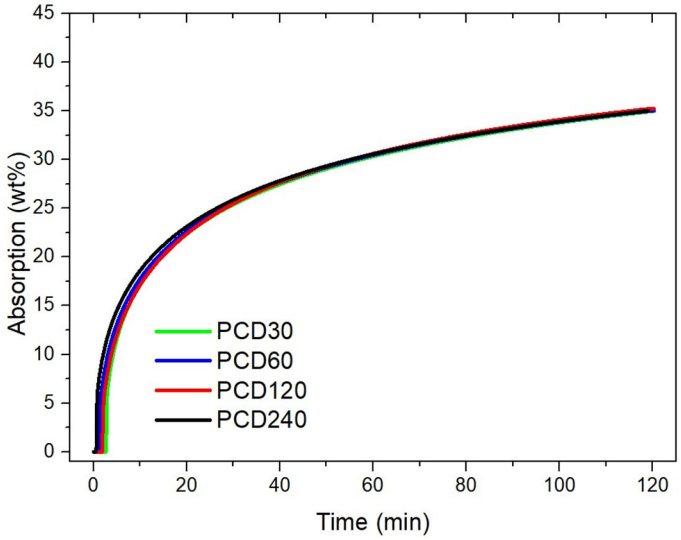


Figure 3. CO_2 uptake performance of calcined (900 °C) dolomite at 450 °C for different isothermal times.

3.6. Sorption Performance, CO_2 Concentration Effect, and Multicycle Tests

3.6.1. The Sorption Performance of the Thermally Pre-Treated Dolomite

Given the CO_2 uptake performance recorded for the calcined dolomite samples, and PCD60 exhibiting the best textural and morphological properties (Tables 1 and 2, and Figure 1), the PCD60 sample underwent thermal pre-treatment (activation) under an inert atmosphere, as documented in Section 2.1.1. Subsequently, the prepared sample (PCD60Act) was examined under a range of CO_2 sorption temperatures (300–800 °C) to determine the optimum sorption temperature and operating conditions. Figure 4 shows that CO_2 sorption improves with increasing temperature, reaching an optimal uptake at 650 °C, with approximately 0.477 $g_{CO2}/g_{sorbent}$ CO_2 uptake. Above 650 °C, the sorption performance steadily declines.

Several tests were performed to compare the CO_2 sorption capacity on all the activated PCD samples (PCD30Act, PCD60Act, PCD120Act, and PCD240Act) at the optimal CO_2 sorption temperature, as established in Figure 4 (650 °C). Figure 5a shows that PCD60Act exhibited the highest CO_2 sorption capacity compared to the others. This performance is attributed to a favorable balance between the decomposition of carbonates during calcination and the preservation of the material's crystalline defects upon activation. Therefore, the 60 min calcination time was selected as optimal, as it showed the best CO_2 capture capacity while also representing a practical compromise, requiring a shorter processing time and lower energy consumption compared to longer calcination times, as confirmed by the energy consumption analysis of the quartz cylindrical furnace (Table S2).

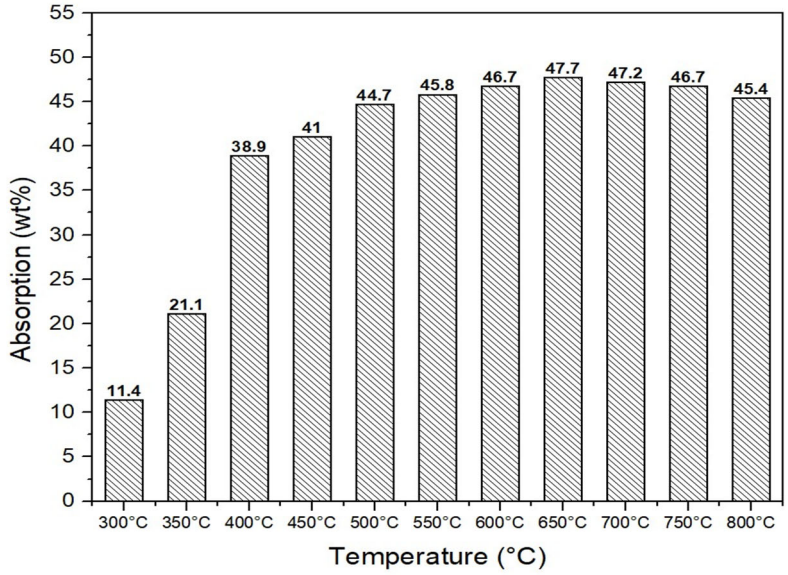


Figure 4. CO_2 uptake performance of PCD60Act at different sorption temperatures after 30 min.

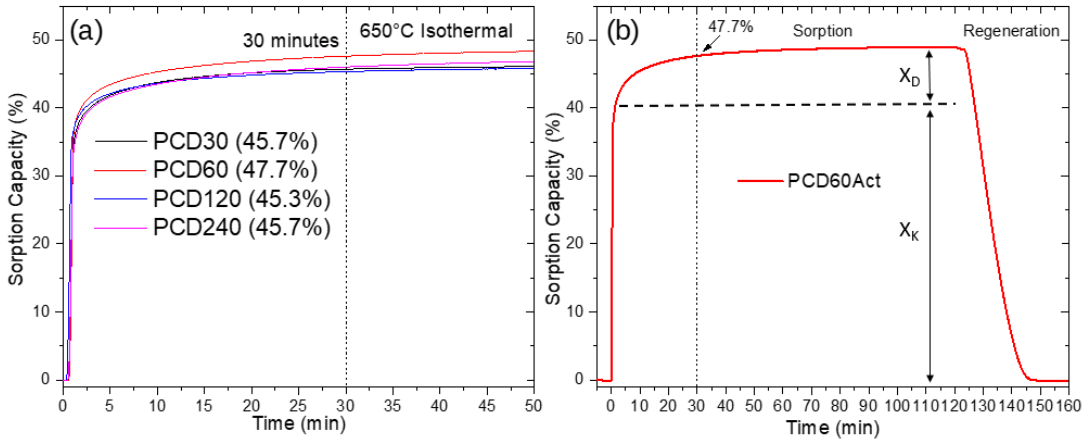


Figure 5. (**a**) CO_2 uptake performance of activated PCD samples at 650 °C and (**b**) isothermal sorption–regeneration kinetics of activated PCD at 650 °C. Vertical dashed line denotes the 30 min. weight % increase in the intersect of red curve (weight %, sorption capacity), while the horizontal dashed line denotes the weight % limit between the kinetic (X_K) and diffusional (X_D) regions, respectively.

Likewise, consistent with the representative curve presented in Figure 5b, the sorption process for activated PCD samples occurred rapidly initially (kinetically controlled, X_K), making the first 5 min the most crucial, and then slowly, especially from the 15 min mark (diffusion-controlled, X_D), while the CO_2 sorption reached saturation. This feature proves to be an important advantage, as in real-world conditions typical of industrial settings (limited CO_2 concentrations and elevated gas flow rates), carbon capture predominantly occurs during the kinetically controlled phase [6]. This behavior can be attributed to fast kinetics driven by the availability of basic functional sites on the surface of the sorbent, resulting in a more efficient gas–solid interaction between the sorbent and the CO_2 atmosphere for improved uptake, considering that the favorable morphology theoretically accommodates more active sites, together with a solid porous network [72].

Additionally, Figure S5 illustrates the CO_2 sorption capacities observed across the three PCD60Act replicates (47.3%, 47.7%, and 47.5%), yielding a mean value of 47.5% with a remarkably small standard deviation of 0.23%. This corresponds to a relative standard deviation (RSD) of just 0.48%, showing minimal scatter between measurements. Such low variability highlights the precision of the experimental setup used in this study, particularly

the stability of the inert atmosphere and temperature control during testing. Also, CO_2 sorption capacities at different CO_2 concentrations (70, 80, and 90%) were studied and are presented in Figure S6. As expected, the CO_2 uptake performance at 90% CO_2/Ar had the best capacity, while the uptakes of 70% and 80% CO_2 concentrations remained consistent (≈0.43 $g_{CO2}/g_{sorbent}$), highlighting the outstanding capture capacity of the PCD60Act regardless of the CO_2 concentration.

3.6.2. Multicycle Tests of the Thermally Pre-Treated Dolomite Sorbent

Due to the CO_2 uptake activity of PCD60Act in comparison to other activated PCD samples (PCD30Act, PCD120Act, and PCD240Act) at a CO_2 sorption temperature of 650 °C, a multicyclic (15) sorption–regeneration study was conducted using temperature-swing sorption (TSS) at 450 °C (isothermal 60 min) and 650 °C (isothermal 15 min) for sorption (90% CO_2 atmosphere) and regeneration (100% Ar atmosphere), respectively, as shown in Figure 6a. According to the thermogram, the sorption process for PCD60Act at 450 °C occurred mainly in the diffusion-controlled phase, taking a longer saturation time for the formation of the carbonate product layer. This behavior is a departure from the sorption of PCD60Act at 650 °C, which was characterized by a kinetically controlled phase (Figure 5). PCD60Act at 450 °C recorded 0.27 $g_{CO2}/g_{sorbent}$, 0.24 $g_{CO2}/g_{sorbent}$, and 0.22 $g_{CO2}/g_{sorbent}$ during the first three CO_2 sorption–regeneration cycles, respectively, showing an obvious degradation behavior with cycle increase. With each cycle increase, the sorbent degradation reduced relatively until stable at the 11th cycle (0.19 $g_{CO2}/g_{sorbent}$). A mild recovery was noticed in the 13th and 14th cycle, registering 0.20 $g_{CO2}/g_{sorbent}$ and 0.21 $g_{CO2}/g_{sorbent}$, respectively.

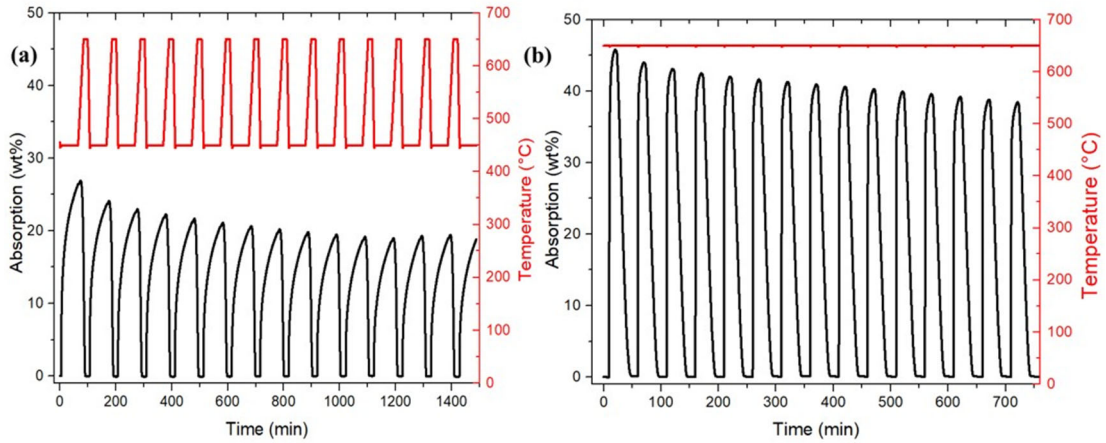


Figure 6. (**a**) Multicyclic test of PCD60Act at 450 °C and (**b**) isothermal multicyclic tests of PCD60Act at 650 °C.

Drawing a contrast between the multicyclic tests of PCD60Act using two different operating conditions, TSS as in Figure 6a and isothermal sorption–regeneration (Figure 6b), the results show that isothermal sorption–regeneration at 650 °C is the optimum for outstanding kinetically controlled sorption performance and enhanced stability over 15 cycles, compared to the lower CO_2 uptake capacity and pronounced sorbent deactivation of the diffusion-controlled TSS operating conditions over multicycles. The multicyclic CO_2 capture performance of the sorbents evaluated under isothermal conditions at 650 °C involved a 10 min sorption phase in a 90% CO_2/Ar atmosphere and a 40 min regeneration phase in pure argon (Section 2.1.2).

Furthermore, Figure 7 illustrates the multicyclic performance of PCD60Act in comparison with that of pristine CaO and UD. The PCD60Act sorbent demonstrated superior cyclic stability, achieving an initial uptake of 0.46 $g_{CO2}/g_{sorbent}$ and retaining 84% of its initial

capacity (0.38 $g_{CO2}/g_{sorbent}$) after 15 cycles. In contrast, while UD exhibited a comparable initial capacity (~0.46 $g_{CO2}/g_{sorbent}$), it degraded more rapidly, retaining only 73% of its capacity by the 15th cycle. Pristine CaO performed least effectively, with an initial uptake of 0.34 $g_{CO2}/g_{sorbent}$ and a retention of 47% (0.16 $g_{CO2}/g_{sorbent}$) after cycling.

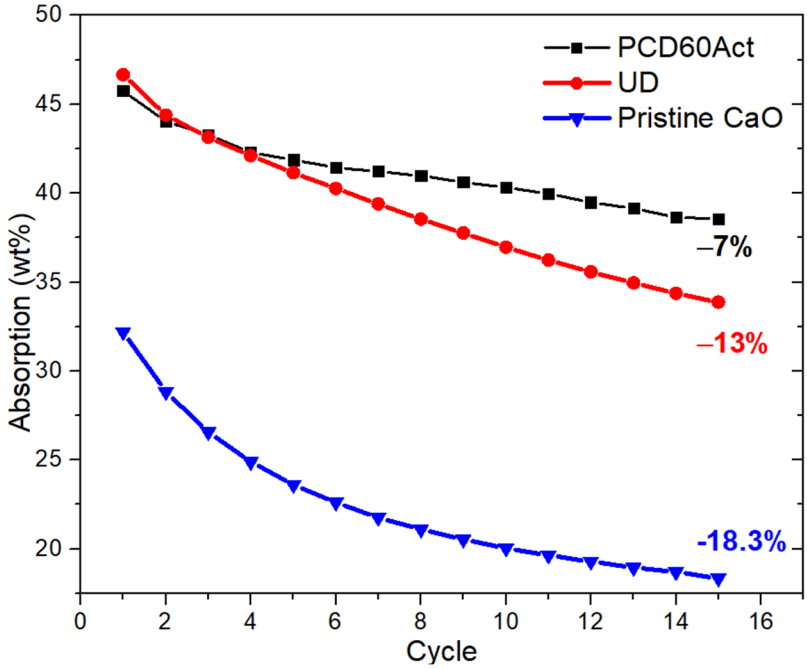


Figure 7. Isothermal multicyclic tests of PCD60Act, UD, and pristine CaO at 650 °C.

The PCD60Act sorbent exhibited significantly lower capacity loss (7 wt%) after 15 cycles compared to UD (13 wt%) and pristine CaO (~18 wt%), showing the effectiveness of thermal pre-treatment in mitigating degradation. This enhanced stability, coupled with its high CO_2 capture capacity, emphasizes the role of dolomite-derived mixed oxides (PCD60Act) in addressing sintering-driven deactivation—a major limitation of conventional CaO-based sorbents. The smaller crystallite sizes, elevated defect density (Tables 1 and 2), and point defects induced by thermal pre-treatment likely delayed structural collapse during cycling, preserving active sites for sustained CO_2 uptake.

Compared to the SEM image of fresh PCD60 (Figure 1c), the relative deactivation of PCD60Act's sorption capacity with each cycle is corroborated by the SEM micrograph (Figure 1d,e) after 15 cycles, as the particles present fracture, larger grains, and aggregation, primarily attributed to the partial formation of agglomerates and the onset of sintering [49], although the porous structure appears somewhat unaltered, maintaining a surface area of 23 m^2/g. Also, Figure S1c shows the particle size distribution for PCDAct60 after 15 sorption–regeneration cycles. Compared with the as-prepared fresh PCD60 with particles ~200 nm, the growth of the particles to over 650 nm emphasizes the net effect of multicyclic tests on the presumable deactivation of the CO_2 sorbent.

Apart from the decline in surface area and pore volume, the modest growth of the MgO crystallite size (29 nm) of the PCD60Act sorbent after 15 cycles compared to that of fresh PCD60 (25 nm) is further evidence of mild sintering. The results demonstrate that while MgO serves as a structural stabilizer and the 650 °C isothermal conditions mitigate sintering during cyclic operation, preserving sub-50 nm CaO crystallite sizes post calcination (e.g., 41 nm for PCD60, Table 1) is critical to minimizing capacity loss. This synergy between MgO stabilization, optimized thermal conditions, and the high dislocation

density of CaO (Table 2) addresses the intrinsic sintering limitations of bulk CaO-based sorbents [73].

3.7. Microstructural and Spectroscopic Characterizations

3.7.1. Fourier-Transform Infra-Red Spectroscopy

In Figure 8a, carbonated PCD60Act presents a prominent absorption peak of CO_3^{2-} at 1396 cm^{-1}, attributed to the asymmetric bond stretching mode (v_3) of the C–O bond [74,75], whereas the CO_3^{2-} peaks at 1089 cm^{-1}, 872 cm^{-1}, and 710 cm^{-1} represent the symmetric stretching (v_1), asymmetric bending (v_2), and symmetric bending (v_4) modes, respectively [76]. The bending vibrational modes v_2 and v_4 present as narrow and sharp, while the v_3 band features as strong and broad. In contrast, the symmetric stretching (v_1) band exhibits a very weak intensity.

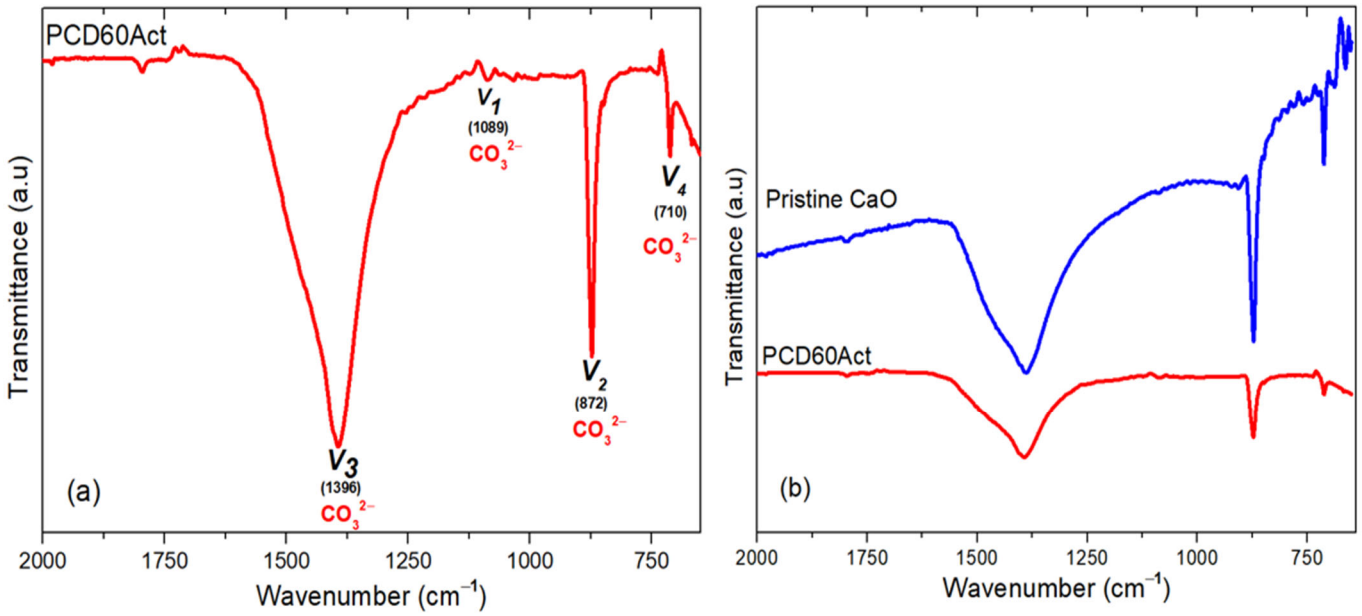


Figure 8. FTIR spectra of carbonated samples (**a**) PCD60Act and (**b**) pristine CaO.

The symmetric stretching (v_1) absorption band, generally forbidden for calcite-group carbonates, can sometimes appear in the FT-IR profile of poorly formed samples or materials whose configuration has been altered by pulverizing [77,78]. In the context of carbon-capture materials, weakly crystallized structures provide several advantages, with energy efficiency during regeneration being the most significant. These materials generally require less energy to regenerate, as their less rigid structure makes it easier to desorb CO_2, typically through heating or reducing the CO_2 partial pressure [79,80]. Therefore, the combined effects of the controlled sintering provided by the dormant MgO skeleton and the improved rate of CO_2 removal by CaO, attributed to the presence of the symmetric stretching (v_1) absorption band (1089 cm^{-1}) as depicted in Figure 8a, presumably lower the minimum temperature needed for full regeneration of PCD60Act in a short residence time, and additionally, the reduced regeneration temperature helps to mitigate sorbent deactivation [81,82].

Figure 8b illustrates the FT-IR spectra comparison of the carbonated samples of PCD60Act and pristine CaO. The spectrum of carbonated PCD60Act exhibits similar peaks to that of carbonated pristine CaO. Thus, the presence of the symmetric stretching (v_1) absorption band at 1089 cm^{-1} observed in the carbonated pristine CaO may be attributed to the same heat pre-treatment regime as in the case of carbonated PCD60Act. However,

the complete regeneration of carbonated pristine CaO is kinetically slower compared to that of PCD60Act, a difference believed to be influenced by the nature of the precursor.

3.7.2. Powder X-Ray Diffraction

Figure 9a demonstrates the major phases present after the carbonation of PCD60Act, confirming that MgO is inert, and only CaO was involved in the CO_2 sorption reaction. Due to its high Tammann temperature, MgO serves as an inactive framework that inhibits the growth and clustering of CaO crystallites [83]. Figure S7 depicts the XRD reflections of fresh dolomite for comparison.

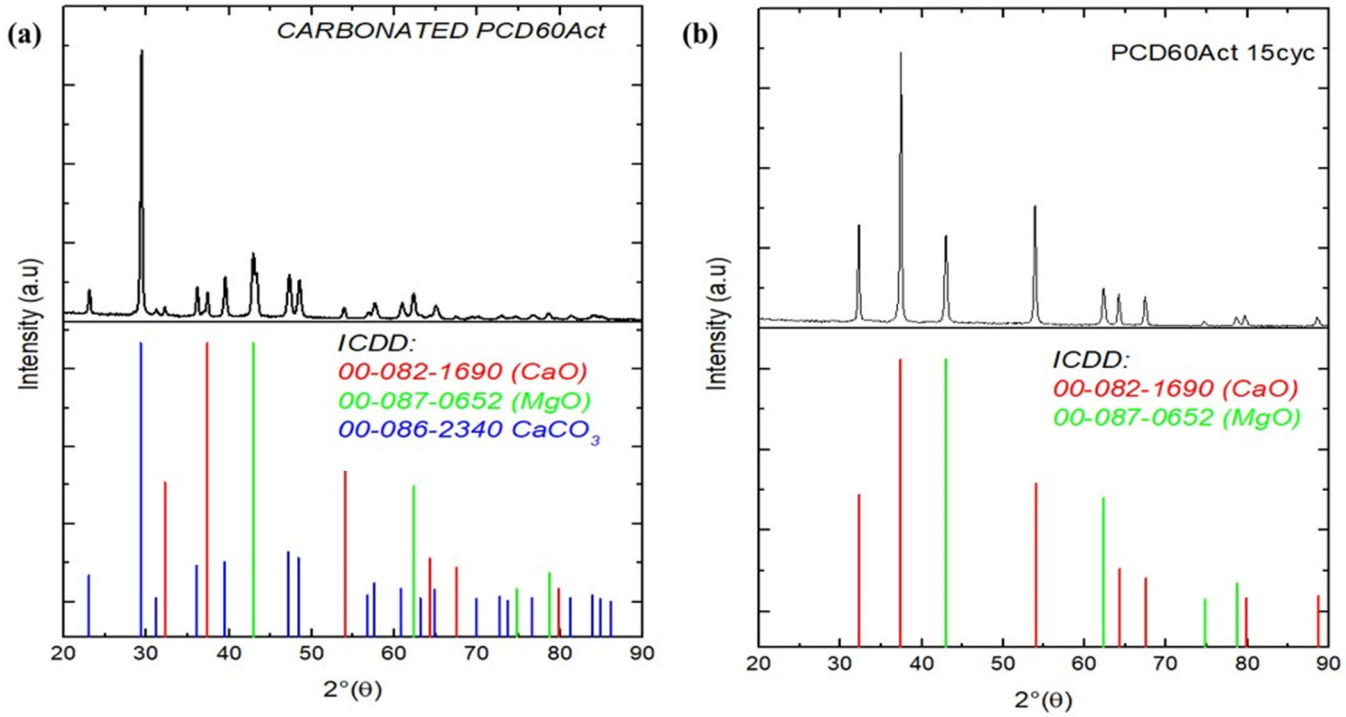


Figure 9. XRD of (**a**) carbonated PCD60Act at 650 °C and (**b**) PCD60Act after multicyclic tests.

Yang et al. [57] claimed that to enhance the CO_2 sorption efficiency of a CaO-bearing natural sorbent with MgO, the MgO composition should be at least 31.5%. Thus, a naturally occurring CaO–MgO sorbent with a MgO composition ranging from 31.5% to 38.7% is believed to be ideal for outstanding CO_2 capture, a range that surpasses the MgO composition in fabricated CaO–MgO sorbents [23,37,84]. Through the Rietveld refinement of the XRD of the calcined CaO-based dolomite sorbent (PCD60), Figure S8 illustrates a MgO content of 38%, supporting earlier statements.

The diffractogram in Figure 9b depicts the successful complete regeneration of the major CaO–MgO phases of PCD60Act after 15 sorption–regeneration cycles. This notable recovery shows the durability of the as-prepared sorbent and the availability of pores for cyclic CO_2 uptake. The presence of passive MgO in the CaO-based sorbent promotes the formation of a robust skeletal structure, enhancing the sorbent's regenerability and stability over multiple cycles under modest conditions [85,86].

Moreover, the XRD patterns of PCD60 and PCD60Act were analyzed using Rietveld refinement to extract quantitative microstructural parameters, including crystallite size and lattice strain (Figure S9). The presence of $Ca(OH)_2$ was observed in both samples, due to hygroscopicity (Figure S9a). Also, a systematic increase in CaO crystallite size was presented in PCD60Act (93.4 nm) compared to PCD60 (85.5 nm), with same trend noted in the MgO crystallite sizes of both samples as well. Concurrently, lattice strain

values (Figure S9b) also showed an increasing pattern—from 6% for PCD60 to 18.67% for PCD60Act.

This analogous behavior between crystallite size and lattice strain, though unusual but not impossible, suggests that the inert thermal pre-treatment of the PCD60Act sample could facilitate the formation of **oxygen vacancies** within the CaO and MgO lattices, thereby promoting localized lattice distortions and contributing to increased lattice strain [87].

3.7.3. Raman Spectroscopy

Figure 10a presents the Raman spectroscopy results for the calcined PCD60, UD, and PCD60Act samples. The comparative analysis reveals similar behavior in the three samples and detects a significant spectral modification in the characteristic CaO peak observed at ~792 cm^{-1}, induced by calcination of PCD60 and the thermal treatment procedure in PCD60Act sample. Although the cubic structure of CaO and MgO present in the calcined dolomite does not show first-order Raman modes in its original state, it does show second-order Raman modes [88]. The peaks observed in all samples are attributed to the characteristic CaO and $Ca(OH)_2$ (~300, ~792 and ~1054 cm^{-1}) [89,90] and MgO (~160, ~481, ~690, ~1340 cm^{-1}) [88,91] phases derived from calcined dolomite. The CaO peaks overlap with the $Ca(OH)_2$ peaks due to the high hygroscopicity of the materials. Additionally, the trace spectra of $CaCO_3$ (~1054 cm^{-1}) and $Ca(OH)_2$ (~1206 cm^{-1}) indicate partial carbonation and hydroxylation due to environmental exposure to moisture and atmospheric CO_2.

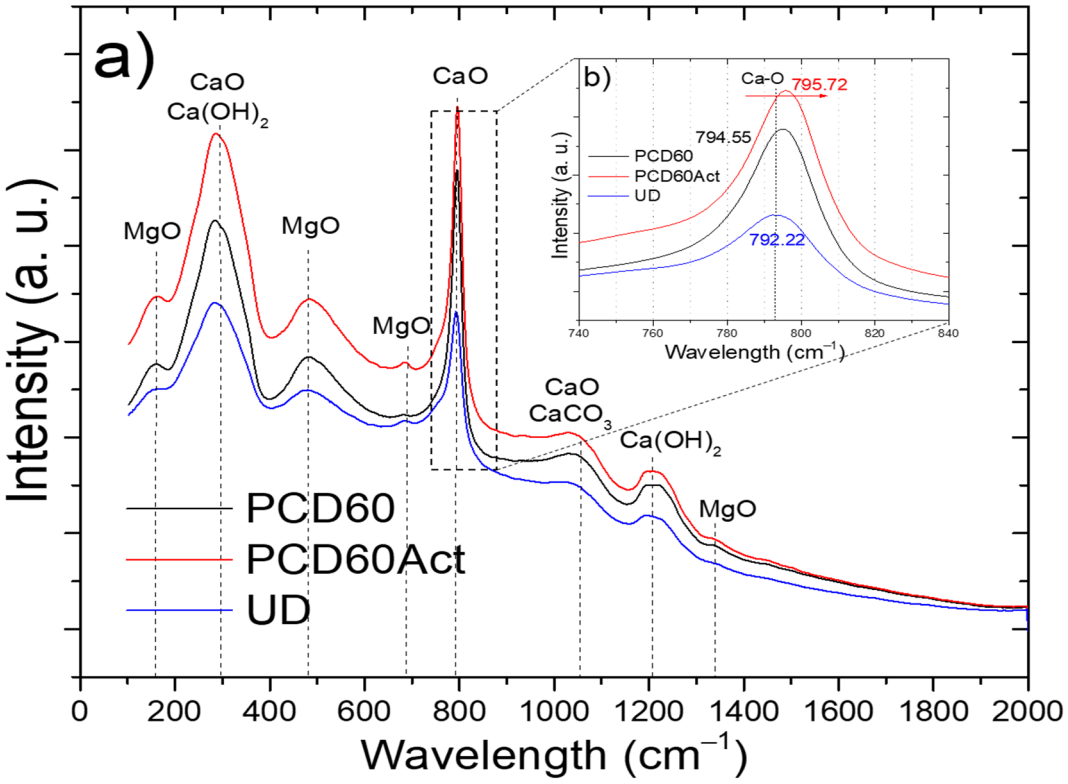


Figure 10. Raman spectra of (**a**) PCD60, UD, and PCD60Act, and (**b**) magnified view of CaO peak at 792.22 cm^{-1}. The red arrow in the inset (**b**) represents a shift of the wavelength towards higher values due oxygen vacancies in sample PCD60Act compared to PCD60 and UD samples.

On the other hand, of particular interest is the peak at 792.22 cm^{-1}, corresponding to Ca-O vibrations in CaO, which is shown in detail in the magnified view as an inset (Figure 10b). This peak is exclusively attributed to the CaO phase, as it does not appear in the spectra characteristic to the $Ca(OH)_2$ hydrated phase [89,92]. Thermal pre-treatment

in an inert atmosphere (activation) induces a significant shift for PCD60Act, revealing key information about structural defect formation (oxygen vacancies) in the CaO crystal lattice. This characteristic shift of the peak located at 792.22 cm^{-1} (Ca-O) towards the higher wavenumber (blueshift) 795.72 cm^{-1} (+3.5 cm^{-1}) is attributed to the vibrations of Ca^{2+} ions near oxygen vacancies, and indicates the emergence of lattice strain for compression [93], as supported by the Rietveld refinement (Figure S9b). In this case, the phenomenon results from two main mechanisms: local tensile and compressive strain variation in the lattice around oxygen vacancies [93], and charge redistribution associated with oxygen vacancies, which modifies interatomic interactions.

Earlier investigations by Parker and Siegel [94] and Wellner et al. [95] reported similar conclusions for TiO_2 and Ge nanocrystals, respectively. Our results demonstrate that inert-atmosphere thermal pre-treatment enabled the generation of oxygen vacancies that directly influenced the CO_2 sorption capacity of the PCD60Act sample.

3.7.4. X-Ray Photoelectron Spectroscopy

The XPS survey scan of fresh dolomite verified the presence of oxygen, magnesium, calcium, and carbon elements (Figure 11a), while the C 1s peak is for adventitious carbon (reference carbon). The analysis also indicates that Mg 1s has the highest binding energy, measuring 1303 eV (Figure 11b), compared to the binding energies of individual elements in the material [96]. Furthermore, the approach for curve approximation for the orbital pair components in Ca $2p_{3/2}$ and $2p_{1/2}$ showed positioning at 347 eV and 350.5 eV, respectively, indicating spin-orbital splitting that is characteristic of calcium-containing compounds (Figure 11c) [38,96]. Figure 11d shows the O 1s region, with the two components O_1 (64%) and O_3 (36%) corresponding to lattice oxygen and the OH^- group, respectively.

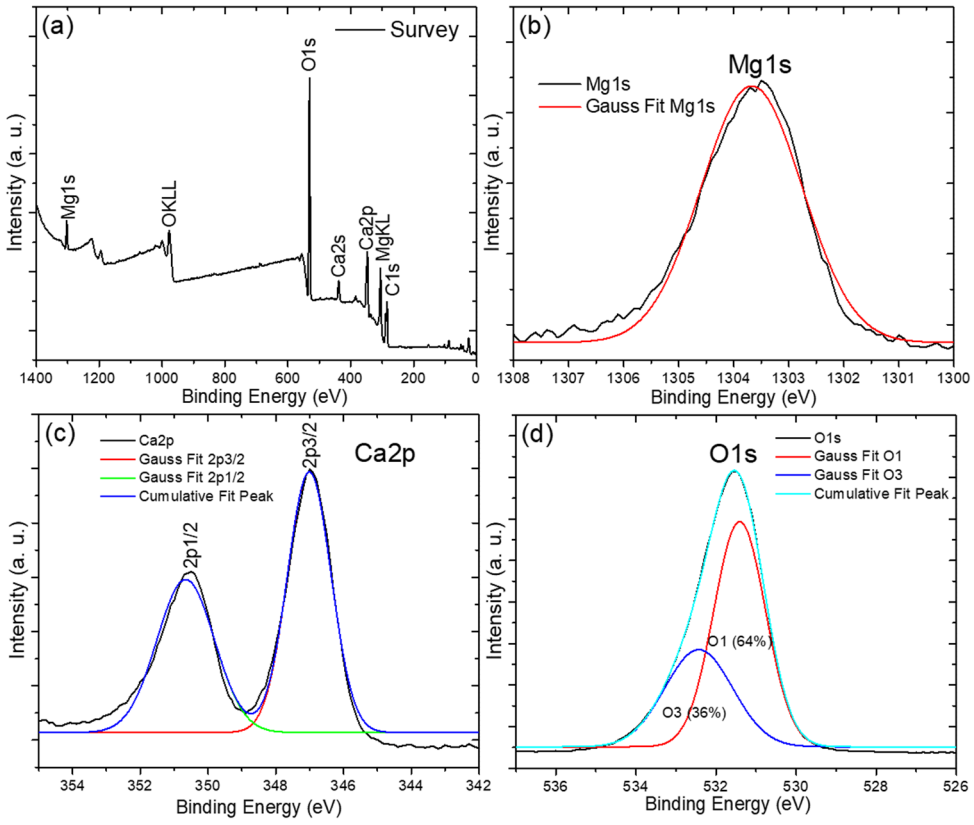


Figure 11. XPS spectra of (**a**) fresh dolomite survey scan, (**b**) Mg 1s, (**c**) Ca 2p, and (**d**) O 1s.

As shown in Figure 12a, the oxygen O 1s spectrum of PCD60Act is deconvoluted into three peaks. The maximum at 530.5 eV represents lattice oxygen (O_1) and the peak at

533.5 eV indicates to hydroxyl group surface-adsorbed oxygen (O_3) [97,98]. The highest contribution for this sample comes from O_2 at 531.7 eV, which is linked to the number of surface oxygen vacancies, which are critical for the CO_2 sorption reaction efficiency of Ca-rich compounds [99,100]. The contributions of the different oxygen species are shown in Figure 12b. The greatest contribution of an oxygen type comes from O_2 related to oxygen vacancies, with 51%, followed by lattice oxygen, with 35%, and the lowest contribution comes from O_3, with 14%. These latter results suggest that thermal pre-treatment of sample PCD60Act effectively increased the O_2 content in the dolomite precursor, enhancing its CO_2 capture capabilities. Comparing the oxygen O 1s spectrum of PCD60Act with that of UD (Figure 12c), the data show that the lattice oxygen type (O_1) is the primary component, located at 531.5 eV, matching the results for fresh dolomite (Figure 11d), while the other oxygen type (O_3) corresponds to the OH^- group. Also, Figure 12d shows the contributions of oxygen types for the UD sample, exhibiting 90 and 10% for O_1 and O_3, respectively. These results conclusively remark the high O_2 concentration of the PCD60Act sample, suggesting the formation of a significant amount of surface oxygen vacancies due to the inert thermal pre-treatment that this sample was exposed to.

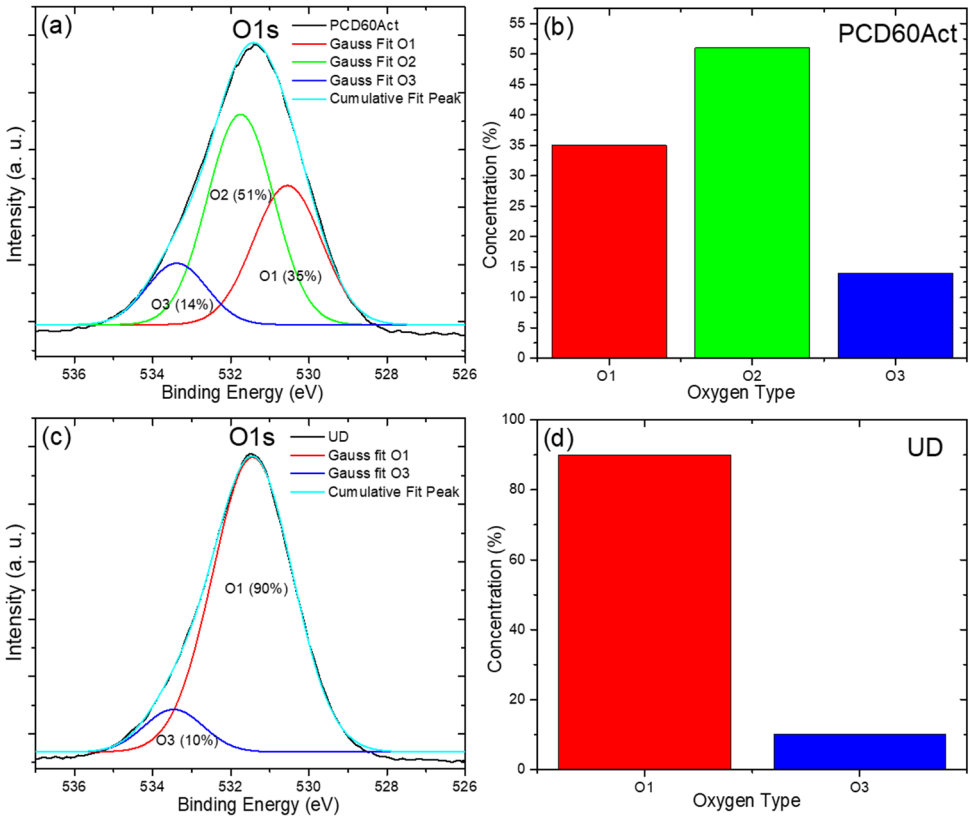


Figure 12. XPS spectra of (**a**) O 1s for PCD60Act, (**b**) concentrations for O_1 oxygen (red), O_2 oxygen (green), and O_3 oxygen (blue) species for PCD60Act, (**c**) O 1s for UD, and (**d**) concentrations for O_1 oxygen (red) and O_3 oxygen (blue) species for UD.

3.7.5. Ultraviolet-Visible Spectroscopy

The absorption band in the UV-vis region corresponds to the band gap energy associated with electronic transitions from the valence band to the conduction band [69]. Hence, the direct band gap energies of the as-prepared samples can be estimated based on these electronic transitions, as illustrated by the Tauc plot in Figure 13.

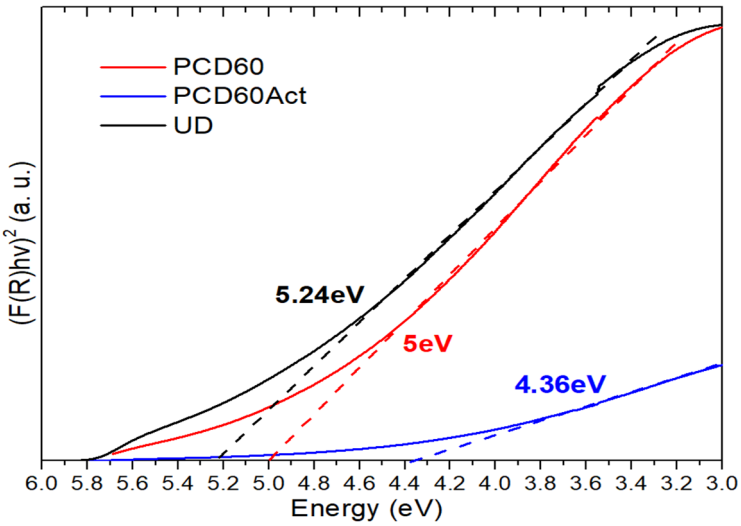


Figure 13. Estimated band gap energies of PCD60, PCD60Act, and UD.

A comparative analysis of the optical band gap energies in Figure 13 reveals a decreasing trend in the following order: UD (5.24 eV) > PCD60 (5.00 eV) > PCD60Act (4.36 eV). The progressive narrowing of the band gap is attributed to the increasing concentration of oxygen vacancies, particularly pronounced in PCD60Act due to the inert-atmosphere thermal pre-treatment, which promoted defect formation and introduced localized states within the band structure.

This trend shows the significant influence of the thermal treatment atmosphere and sequence on the electronic structure of the materials, as corroborated by the Raman spectra (Figure 10). The existence of density dislocation, as estimated and presented in Table 2, demonstrates the effect of open-air calcination on the generation of line defects on the surface of PCD60. However, further thermal pre-treatment in argon leads to enhanced point defects, oxygen vacancies, evidenced by the narrowing of the band gap of PCD60Act (Figure 13), with a band gap energy reduction of 0.88 eV and 0.64 eV compared to UD and PCD60, respectively. These generated oxygen vacancies introduce localized electron-rich states within the band gap, positioned just below the conduction band edge. Such defect states effectively reduce the optical band gap by facilitating lower-energy electronic transitions, thereby enhancing the material's properties [101].

Numerous theoretical investigations have been conducted to elucidate the role of crystalline defects in facilitating CO_2 activation and its subsequent conversion into value-added products. Thompson et al. [102] and Rawool et al. [103] demonstrated that oxygen vacancies contribute to narrowing the band gap in pristine TiO_2 and enhance the formation of strong sorption sites for CO_2 capture and activation. In a related study, Zhu et al. [104] synthesized oxygen-deficient CeO_2 (CeO_2–V_0) by annealing CeO_2 under an inert atmosphere, effectively introducing oxygen vacancies into the lattice.

Ultimately, point defects—particularly oxygen vacancies—play a critical role in modulating the band gap energy, where a reduced band gap facilitates electron excitation from the valence band to the conduction band with lower energy input. This defect engineering offers an effective strategy to optimize CaO-based sorbents for CO_2 capture by lowering the effective band gap, generating CO_2-reactive surface sites, and enhancing charge transfer for sorption kinetics.

4. Role of Crystalline Defects

The enhanced CO_2 uptake performance of the prepared PCD60Act sorbent was linked to the generation of defects (oxygen vacancies) formed during the thermal pre-treatment of

the dolomite sample via activation upon exposure to an argon atmosphere before attaining the sorption (carbonation) temperature of 650 °C. Oxygen vacancies in CaO-based sorbents are critical for generating basic defect sites that improve CO_2 sorption performance, as demonstrated by experimental and theoretical studies. These vacancies, introduced via thermal pre-treatment or doping, act as catalytically active sites that promote O^{2-} ion migration and lower energy barriers for CO_2 chemisorption. For instance, in CeO_2-doped CaO sorbents, Ce^{3+}/Ce^{4+} redox activity generates oxygen vacancies, accelerating O^{2-} transport and increasing the CO_2 capacity by 43% compared to undoped CaO [105]. Similarly, Na_2CO_3-doped CaO introduces oxygen vacancies through Na^+ substitution, stabilizing defect sites and reducing the activation energy for CO_2 sorption [106]. Additionally, thermal pre-treatment, such as calcination, further enhances vacancy formation. In hydrocalumite-derived CaO-$Ca_{12}Al_{14}O_{33}$ systems, high-temperature treatment (800–950 °C) induces oxygen vacancies in the mayenite structure, enabling rapid O^{2-} diffusion through the $CaCO_3$ layer and improving cyclic stability [107]. This aligns with the PCD60Act dolomite sorbent, where thermal pre-treatment generates oxygen vacancies, as confirmed by XRD, XPS, Raman, and UV-vis spectroscopy, leading to enhanced CO_2 uptake. XRD, XPS, Raman, and UV-vis analyses confirm lattice strain, oxygen vacancy generation, wavelength shift, and band gap narrowing, respectively, directly correlating vacancy concentration with sorption performance, validating the role of these vacancies as active sites for CO_2 binding. Therefore, oxygen vacancies in CaO-based materials enhance CO_2 capture by optimizing ion mobility and reaction kinetics, with thermal and doping strategies offering scalable routes for defect engineering. The PCD60Act sorbent exemplifies this mechanism, with vacancy generation during thermal pre-treatment supporting its improved CO_2 sorption.

Since the interaction between CO_2 and metal oxides is assumed to proceed mainly via the highest occupied molecular orbital–lowest unoccupied molecular orbital (HOMO-LUMO) pathway [108], the type of carbonate species formed is influenced by the coordination number of the surface oxygen [109]. The LUMO of CO_2 has the maximum energy among the two engaging frontier orbitals. However, as the coordination number decreases, the HOMO energy level of surface oxygen rises. As a result, the HOMO-LUMO energy gap separating O^{2-} and CO_2 is smaller at defect regions, leading charge migration from O^{2-} to CO_2 to materialize at a minimal energy cost for three-coordinated (O_{3C}) and four-coordinated (O_{4C}) sites in contrast to typical five-coordinated (O_{5C}) sites [109,110]. The elevated density of these low-coordinated (O_{3C} and O_{4C}) edges and corner defect sites in PCD60Act must have resulted from the thermal pre-treatment process, which is believed to have induced greater disorder in the crystalline structure of the CaO-based dolomite sorbent [68,70]. Also, the reduced regeneration temperature (650 °C) observed in the dolomite (i.e., PCD60Act) can be attributed to the high density of defects generated during the calcination, which lowered the energy barriers for CO_2 regeneration. The small crystallite sizes (CaO: 41 nm; MgO: 25 nm) and elevated dislocation density ($\rho = 60 \times 10^{10}$ m^{-2} for PCD60, Table 2) indicate a high concentration of structural imperfections, including low-coordinated oxygen sites (O_{3C} and O_{4C}) at defect regions. These sites exhibit a smaller HOMO-LUMO energy gap compared to regular O_{5C} sites, as the HOMO energy of surface oxygen increases with a decreasing coordination number ($O_{3C} > O_{4C} > O_{5C}$) [109,110]. This reduced energy gap facilitates charge transfer during CO_2 sorption and regeneration, lowering the activation energy required for both processes, as corroborated by UV-vis (Figure 13). Also, the abundant defects in PCD60, quantified via dislocation density ($\rho = 1/D^2$, where D = crystallite size), create a disordered crystalline structure with metastable carbonate intermediates. These intermediates, formed at defect-rich regions, are bound less strongly than those on pristine surfaces, enabling CO_2 release at milder regeneration temperatures. Therefore, the calcination and inert thermal pre-treatment of dolomite generates a defect-

rich CaO–MgO framework with optimized surface chemistry (low-coordinated O^{2-} sites) and microstructure (small crystallites, high porosity). These features collectively lower the energy needed for breaking Ca-O-CO_3 bonds during regeneration, enabling efficient sorbent regeneration at reduced temperatures.

5. Proposed Carbon-Capture Mechanism

To clarify the viability of the PCD60Act as a sorbent with crystalline defects in CO_2 capture, a comprehensive understanding of the Ca-O-CO_2 interplay is necessary. Recent computational studies [111–113] have confirmed that CO_2 is sorbed as monodentate carbonate (CO_3^{2-}) on the edges and corners of low-coordinated O^{2-} sites on CaO. CaO crystals, which present a cubic lattice system with a low Madelung potential, lead to a diffuse electron cloud, inducing interaction with CO_2 [109]. This process occurs in the presence of an oxygen-vacancy point defect, with the top O-site of the defect being the most favorable for CO_2 sorption [111,112,114]. Bearing in mind the provision of a skeletal framework by MgO, below is a plausible illustration of the PCD60 sorption mechanism:

$$\text{MgO•Ca-O-CO}_2\text{ interface: MgO•[Ca}^{2+}\cdots\text{O}^{2-}\text{] + CO}_2 \quad \text{(Step 1)}, \tag{6}$$

$$\text{MgO•[Ca}^{2+}\cdots\text{O}^{2-}\text{] + CO}_2 \rightarrow \text{MgO•[Ca}^{2+}\cdots\ \text{CO}_3{}^{2-}\text{]} \quad \text{(Step 2)}, \tag{7}$$

$$\text{MgO•[Ca}^{2+}\cdots\ \text{CO}_3{}^{2-}\text{]} \leftrightarrow \text{MgO•CaCO}_3 \quad \text{(Step 3)}, \tag{8}$$

Given the generation of crystalline defects (oxygen vacancies) via the thermal pre-treatment procedure, as corroborated by the XRD, XPS, Raman and UV-vis analyses, the presence of the low-coordinated O^{2-} sites yields ion migration and interaction in the CaO–MgO interface in a CO_2 atmosphere (Step 1, 6). The defect-rich CaO–MgO active sites with oxygen vacancies present enhance O^{2-} ion mobility, which induces the sorption of CO_2 as a metastable intermediate (monodentate carbonate), as illustrated in Step 2 (7). Ultimately, Step 3 (8) demonstrates the reversible kinetically controlled chemisorption of CO_2 to form MgO•$CaCO_3$ phases, as confirmed by XRD (Figure 9a).

Furthermore, the calcination of the dolomite sample in an open-air quartz cylindrical furnace, followed by thermal pre-treatment in argon, induces the formation of a special CaO–MgO composite, with the MgO phase imparting structural stability to the material [39,115,116]. During multicyclic CO_2 capture tests, the thermally stable and chemically inert MgO phase acts as a structural stabilizer by spatially separating CaO grains, thereby limiting sintering-induced grain boundary contact. This mitigates deactivation and preserves the cyclic sorption–regeneration performance of the CaO phase, as evidenced in Figure 7.

Table 3 compares the CO_2 sorption capacities of CaO-based dolomite sorbents from the literature with the results of this work. The long-term performance patterns of sorbents can be studied by simulation with realistic CO_2 concentrations. While 15% CO_2 aligns with post-combustion gas streams [73], tests using elevated CO_2 partial pressures (90 to 100% CO_2 concentration) have been reported to accelerate deactivation in CaO-based dolomite sorbents (sintering and pore collapse) over prolonged cycles, thus allowing for rapid assessment of the sorbent's long-term stability under such conditions.

Table 3. Comparison of CO_2 capture capacities of some CaO-based dolomite sorbents.

Sorbent	CaO/MgO Ratio	Calcination Conditions	Sorption Conditions	Regeneration Conditions	Cycles	First–Last Cycle Uptake ($g_{CO2}/g_{sorbent}$)	References
Ball-milled dolomite	Not mentioned	RT-900 °C 300 °C/min, 70% CO_2/30% air	650 °C, 15% CO_2, 85% air	900 °C, 70% CO_2, 30% air	20	0.40–0.27	[73]
Acetic acid-treated dolomite	Not mentioned	900 °C, air, 2 h during preparation; in TGA RT-900 °C 300 °C/min, 70% CO_2/30% air	650 °C, 15% CO_2, 85% air	900 °C, 70% CO_2, 30% air	20	0.29–0.12	[117]
Dolomite	1.64	800 °C, 3 h	690 °C, 15% CO_2	800 °C, 100% N_2	30	0.41–0.17	[118]
Citric acid-treated dolomite	1.64	600 °C, 100% N_2, 2 h and switch 800 °C, air, 3 h	690 °C, 15% CO_2	950 °C, 100% CO_2	20	0.44–0.25	[119]
Dolomite	2.03	800 °C, 100% N_2	700 °C, 15% CO_2	800 °C, 100% N_2	20	0.41–0.27	[39]
Gluconic acid-treated dolomite	1.64	800 °C, air, 2 h	700 °C, 15% CO_2	950 °C, 100% CO_2	10	0.45–0.40	[120]
Dolomite	1.45	Not mentioned	650 °C, 30% CO_2, 10% H_2O	850 °C, 100% N_2	50	0.45–0.26	[25]
Dolomite	55.61 wt% $CaCO_3$, 44.2 wt% $MgCO_3$	RT- 900 °C, 50%CO_2/50% N_2 and switch 900 °C, 100%N_2, 5 min	600 °C, 50% CO_2	900 °C, 100% N_2	15	0.21–0.17	[53]
Dolomite	23.63 wt% Ca, 9.63 wt% Mg	850 °C, N_2, 1 h during preparation; in TGA RT-725 °C 300 °C/min, N_2, 10 min	850 °C, 100% CO_2	725 °C, 100% N_2	20	0.45–0.40	[121]
Dolomite	3.46	RT- 800 °C, 100% N_2, 6 °C/min	700 °C, 100% CO_2	750 °C, 100% N_2	8	0.23–0.18	[122]

Table 3. *Cont.*

Sorbent	CaO/MgO Ratio	Calcination Conditions	Sorption Conditions	Regeneration Conditions	Cycles	First–Last Cycle Uptake ($g_{CO2}/g_{sorbent}$)	References
Dolomite	1.93	800 °C, vacuum	400 °C, 100% CO_2	800 °C, vacuum	3	0.51–0.30	[123]
PCD60Act	1.64	900 °C, air, 1 h during preparation; in TGA RT- 650 °C, 100% Ar, 30 min	450 °C, 90% CO_2	650 °C, 100% argon	15	0.25–0.17	This work
PCD60Act	1.64	900 °C, air, 1 h during preparation; in TGA RT- 650 °C, 100% Ar, 30 min	650 °C, 90% CO_2	650 °C, 100% argon	15	0.44–0.37	This work

For instance, the CO_2 uptake capacity using 15% CO_2 reaches 0.45 $g_{CO2}/g_{sorbent}$ in the 1st cycle, with a rapid capacity loss at the 20th cycle [39,117–119]. Furthermore, the performance in studies using 100% CO_2 varies, stressing that the sintering mechanisms observed under high CO_2 concentrations correlate strongly with real-world performance degradation, justifying accelerated testing protocols [46]. As expected, there are sorbents that deactivate within a few cycles, demonstrating their poor stability [122,123]. But, in our study, using 90% CO_2 retained a CO_2 uptake capacity of 0.38 $g_{CO2}/g_{sorbent}$ after 15 cycles for PCD60Act, compared to the 0.40 gCO_2/gs_{orbent} reported by Han's team [121] after 20 cycles. It is noteworthy to highlight that Han et al.'s [121] study carried out high-temperature cyclic sorption–regeneration with a low-Mg-content dolomite (high CaO:MgO ratio).

Furthermore, the optimal MgO content in synthetic sorbents for CO_2 capture has been a subject of significant research. However, for natural sorbents, the literature is limited. For instance, Yang et al. [57] identified that a 38.7 wt% MgO content in calcined dolomite (corresponding to 17.16 wt% in natural dolomite) yields the best results for CO_2 uptake capacity and cyclic stability. This optimal composition, found in commercially available dolomite from China, demonstrated a CO_2 uptake capacity of 0.45 $g_{CO2}/g_{sorbent}$ in the initial cycle, and maintained stability over 50 cycles, with a CaO:MgO ratio of 1.45 [57].

Comparative studies using natural dolomites from various sources and commercial dolomite with a lower MgO content have shown less favorable results in terms of stability. Japanese natural dolomite (CaO:MgO ratio of 1.93) [123], Chinese natural dolomite (CaO:MgO ratio of 2.45) [121], and Alfa Aesar commercial dolomite (CaO:MgO ratio of 3.4) [122] have all exhibited poor stability similar to that of limestone-based sorbents. In contrast, the calcined Mexican natural dolomite used in the current study contained 38 wt% MgO, resulting in a CaO:MgO ratio of 1.63. This composition aligns with the optimal ratio identified by Yang and co-workers [57], suggesting that the Mexican natural dolomite may be more suitable for CO_2 capture applications, offering improved cyclic stability compared to the other dolomite sources mentioned.

Notably, as far as we know, this is the first documented case of dolomite sorption–regeneration at a minimum temperature of 650 °C with reasonable kinetics. Also, giving consideration to energy consumption, prolonged treatments (e.g., 240 min) significantly increase energy demand, whereas shorter calcination times (e.g., 60 min) balance energy efficiency with performance (Table S2), justifying process scalability. This breakthrough has significant implications for the sorbent's durability, not only under sorption and regeneration conditions for CO_2 capture, but also in other processes, such as gas reforming for hydrogen production with simultaneous CO_2 capture [124–126].

6. Conclusions

This study demonstrates the successful development of a thermally pre-treated dolomite-based sorbent (PCD60Act) for efficient CO_2 capture at moderate temperatures. Calcination of natural dolomite at 900 °C for 60 min, followed by activation under an inert argon atmosphere at 650 °C, generated a defect-rich CaO–MgO composite with exceptional CO_2 uptake and cyclic stability. The PCD60Act sorbent achieved an initial CO_2 capacity of 0.477 gCO_2/gsorbent at 650 °C, and retained 84% of its capacity (0.38 gCO_2/gsorbent) after 15 cycles under isothermal sorption–regeneration conditions. Notably, the regeneration at 650 °C—significantly lower than that of conventional CaO-based systems (>800 °C)—highlights the energy efficiency and practical viability of this approach.

The enhanced performance stems from the synergistic effects of MgO stabilization and defect engineering. Thermal pre-treatment introduced oxygen vacancies and lattice strain, as confirmed by Raman, XPS, and UV-vis analyses, which lowered the energy barrier for CO_2 chemisorption and facilitated rapid sorption–regeneration kinetics. The inert MgO

framework mitigated sintering by spatially isolating CaO crystallites, preserving textural properties (23 m^2/g post-cycling) and dislocation density (60×10^{10} m^{-2}). These structural advantages were further evidenced by XRD and SEM, which revealed retained porosity and suppressed agglomeration after cycling.

A comparative analysis with the current literature showed the superiority of PCD60Act, particularly under high CO_2 concentrations (90%), where it outperformed most dolomite-derived sorbents in capacity retention. The optimal CaO:MgO ratio (1.64) in the Mexican dolomite source aligned with theoretical thresholds for stability, enabling durable performance without costly synthetic modifications.

This work advances the integration of natural mineral sorbents into carbon capture systems, offering a scalable, cost-effective solution for applications such as integrated carbon capture and conversion (ICCC). Its moderate operational temperatures and robust cyclic stability position PCD60Act as a promising candidate for hydrogen production processes (e.g., dry reforming) and industrial flue gas treatment, bridging the gap between energy efficiency and environmental sustainability. Future studies should explore pilot-scale validation and long-term stability under realistic gas compositions to accelerate industrial adoption.

Supplementary Materials: The following supporting information can be downloaded at https://www.mdpi.com/article/10.3390/c11020037/s1, Figure S1: Particle size distributions of (a) PCD240, (b) PCD60, and (c) PCDAct60 after 15 sorption–regeneration cycles; Figure S2: Thermal decomposition study of dolomite in an air atmosphere; Figure S3: Pore size distributions of PCD240 and PCD60; Figure S4: Adsorption–desorption isotherm curves of PCD240 and PCD60; Figure S5: Statistical analysis of three consecutive replicates of PCD60Act; Figure S6: CO_2 uptake performance of PCD60Act at different CO_2 concentrations; Figure S7: X-ray diffraction of fresh dolomite; Figure S8: Rietveld refinement spectra of PCD60; Figure S9: Rietveld Refinement of PCD60 and PCD60Act for quantification of (a) composition and (b) lattice strain; Table S1: Elemental composition of fresh dolomite; Table S2: Quartz cylindrical furnace calcination energy consumption.

Author Contributions: Conceptualization, methodology, investigation, formal analysis, writing—original draft preparation, I.G.A.; methodology, investigation, writing—review and editing, J.E.M.-M.; writing—review and editing, A.B.J.-S.; methodology, investigation, J.L.D.-A.; visualization, B.C.H.-M.; software, H.A.S.; validation, J.L.B.-E.; data curation, L.I.I.-R.; conceptualization, supervision, writing—review and editing, A.L.-O.; project administration, V.H.C.-M. All authors have read and agreed to the published version of the manuscript.

Funding: This research received no external funding.

Data Availability Statement: The original contributions presented in this study are included in the article/Supplementary Material. Further inquiries can be directed to the corresponding author.

Acknowledgments: The authors wish to express their sincere gratitude for the use of facilities and infrastructural support provided by Secretaría de Ciencia, Humanidades, Tecnología e Innovación (SECIHTI) and Centro de Investigación en Materiales Avanzados S. C. (CIMAV), respectively. The authors would also like to express their gratitude to CIMAV staff members Andrés Isaak González Jacquez for the XRD analysis, César Cutberto Leyva Porras for the SEM-EDS analysis, Pedro Pizá Ruiz for the RAMAN and UV-vis spectroscopy, and Luis Gerardo Silva for his support with the XPS analysis.

Conflicts of Interest: The authors declare no conflicts of interest.

Abbreviations

The following abbreviations are used in this manuscript:

ICCC	Integrated carbon capture and conversion
CCU	Carbon capture and utilization
DFM	Dual-function material
DRM	Dry reforming of methane
ICP-OES	Inductively coupled plasma optical emission spectroscopy
TSS	Temperature-swing sorption
SEM-EDS	Scanning electron microscopy–energy-dispersive spectroscopy
XRD	X-ray diffraction
ICDD	International Centre for Diffraction Data
BET	Brunauer–Emmett–Teller
BJH	Barrett–Joyner–Halenda
FT-IR	Fourier-Transform Infra-Red
XPS	X-ray photoelectron spectroscopy
UV-vis	Ultraviolet-visible spectroscopy
TGA	Thermogravimetric analysis
HOMO	Highest occupied molecular orbital
LUMO	Lowest unoccupied molecular orbital

References

1. Li, F.; Hemmati, A.; Rashidi, H. Industrial CO_2 absorption into methyldiethanola-mine/piperazine in place of monoethanolamine in the absorption column. *Process Saf. Environ. Prot.* **2020**, *142*, 83–91. [CrossRef]
2. Skoufa, Z.; Antzara, A.; Milios, I.; Heracleous, E.; Lemonidou, A.A. CaO-Based Sorbents for Post Combustion CO_2 Capture via Carbonate Looping. In *Energy, Transportation and Global Warming*; Springer: Cham, Switzerland, 2016; pp. 571–589. [CrossRef]
3. Samanta, A.; Zhao, A.; Shimizu, G.K.H.; Sarkar, P.; Gupta, R. Post-combustion CO_2 capture using solid sorbents: A review. *Ind. Eng. Chem. Res.* **2012**, *51*, 1438–1463. [CrossRef]
4. Abanades, J.C.; Anthony, E.J.; Lu, D.Y.; Salvador, C.; Alvarez, D. Capture of CO_2 from combustion gases in a fluidized bed of CaO. *AIChE J.* **2004**, *50*, 1614–1622. [CrossRef]
5. Chen, J.; Duan, L.; Sun, Z. Review on the Development of Sorbents for Calcium Looping. *Energy Fuels* **2020**, *34*, 7806–7836. [CrossRef]
6. Heidari, M.; Tahmasebpoor, M.; Antzaras, A.; Lemonidou, A.A. CO_2 capture and fluidity per-formance of CaO-based sorbents: Effect of Zr, Al and Ce additives in tri-, bi- and mono-metallic configurations. *Process Saf. Environ. Prot.* **2020**, *144*, 349–365. [CrossRef]
7. Elvira, G.B.; Francisco, G.C.; Víctor, S.M.; Alberto, M.L.R. MgO-based adsorbents for CO_2 adsorption: Influence of structural and textural properties on the CO_2 adsorption performance. *J. Environ. Sci.* **2017**, *57*, 418–428. [CrossRef]
8. Su, Y.; Han, R.; Gao, J.; Wei, S.; Sun, F.; Zhao, G. Novel method for regeneration/reactivation of spent dolomite-based sorbents from calcium looping cycles. *Chem. Eng. J.* **2019**, *360*, 148–156. [CrossRef]
9. Fedunik-Hofman, L.; Bayon, A.; Hinkley, J.; Lipiński, W.; Donne, S.W. Friedman method kinetic analysis of CaO-based sorbent for high-temperature thermochemical energy storage. *Chem. Eng. Sci.* **2019**, *200*, 236–247. [CrossRef]
10. Gruene, P.; Belova, A.G.; Yegulalp, T.M.; Farrauto, R.J.; Castaldi, M.J. Dispersed calcium oxide as a reversible and efficient CO_2 sorbent at intermediate temperatures. *Ind. Eng. Chem. Res.* **2011**, *50*, 4042–4049. [CrossRef]
11. Abanades, J.C.; Alvarez, D. Conversion limits in the reaction of CO_2 with lime. *Energy Fuels* **2003**, *17*, 308–315. [CrossRef]
12. Sarrión, B.; Perejón, A.; Sánchez-Jiménez, P.E.; Pérez-Maqueda, L.A.; Valverde, J.M. Role of cal-cium looping conditions on the performance of natural and synthetic Ca-based materials for energy storage. *J. CO2 Util.* **2018**, *28*, 374–384. [CrossRef]
13. Benitez-Guerrero, M.; Valverde, J.M.; Sanchez-Jimenez, P.E.; Perejon, A.; Perez-Maqueda, L.A. Multicycle activity of natural $CaCO_3$ minerals for thermochemical energy storage in Concen-trated Solar Power plants. *Sol. Energy* **2017**, *153*, 188–199. [CrossRef]
14. Lan, P.; Wu, S. Synthesis of a Porous Nano-CaO/MgO-Based CO_2 Adsorbent. *Chem. Eng. Technol.* **2014**, *37*, 580–586. [CrossRef]
15. Radfarnia, H.R.; Iliuta, M.C. Metal oxide-stabilized calcium oxide CO_2 sorbent for multicycle operation. *Chem. Eng. J.* **2013**, *232*, 280–289. [CrossRef]
16. Hu, Y.; Liu, W.; Sun, J.; Li, M.; Yang, X.; Zhang, Y.; Xu, M. Incorporation of CaO into novel Nd_2O_3 inert solid support for high temperature CO_2 capture. *Chem. Eng. J.* **2015**, *273*, 333–343. [CrossRef]

17. Ridha, F.N.; Manovic, V.; Macchi, A.; Anthony, M.A.; Anthony, E.J. Assessment of limestone treatment with organic acids for CO_2 capture in Ca-looping cycles. *Fuel Process. Technol.* **2013**, *116*, 284–291. [CrossRef]
18. Li, Y.-J.; Zhao, C.-S.; Duan, L.-B.; Liang, C.; Li, Q.-Z.; Zhou, W.; Chen, H.-C. Cyclic calcina-tion/carbonation looping of dolomite modified with acetic acid for CO_2 capture. *Fuel Process. Technol.* **2008**, *89*, 1461–1469. [CrossRef]
19. Manovic, V.; Anthony, E.J. Carbonation of CaO-based sorbents enhanced by steam addition. *Ind. Eng. Chem. Res.* **2010**, *49*, 9105–9110. [CrossRef]
20. Materić, V.; Symonds, R.; Lu, D.; Holt, R.; Manović, V. Performance of hydration reactivated Ca looping sorbents in a pilot-scale, oxy-fired dual fluid bed unit. *Energy Fuels* **2014**, *28*, 5363–5372. [CrossRef]
21. Valverde, J.M.; Sanchez-Jimenez, P.E.; Perez-Maqueda, L.A. Effect of heat pretreat-ment/recarbonation in the Ca-looping process at realistic calcination conditions. *Energy Fuels* **2014**, *28*, 4062–4067. [CrossRef]
22. Hong, L.; Khan, A.; Pratsinis, S.E.; Smirniotis, P.G. Flame-made durable doped-CaO nanosorbents for CO capture. *Energy Fuels* **2009**, *23*, 1093–1100.
23. Liu, W.G.; Low, N.W.L.; Feng, B.; Wang, G.; Da Costa, J.C.D. Calcium precursors for the production of CaO sorbents for multicycle CO_2 capture. *Environ. Sci. Technol.* **2010**, *44*, 841–847. [CrossRef] [PubMed]
24. Zhang, K.; Li, X.S.; Duan, Y.; King, D.L.; Singh, P.; Li, L. Roles of double salt formation and $NaNO_3$ in Na_2CO_3-promoted MgO absorbent for intermediate temperature CO_2 removal. *Int. J. Greenh. Gas Control* **2013**, *12*, 351–358. [CrossRef]
25. Yang, X.; Zhao, L.; Xiao, Y. Effect of $NaNO_3$ on MgO-$CaCO_3$ absorbent for CO_2 capture at warm temperature. *Energy Fuels* **2013**, *27*, 7645–7653. [CrossRef]
26. Gao, W.; Zhou, T.; Gao, Y.; Louis, B.; O'Hare, D.; Wang, Q. Molten salts-modified MgO-based ad-sorbents for intermediate-temperature CO_2 capture: A review. *J. Energy Chem.* **2017**, *26*, 830–838. [CrossRef]
27. Li, Z.S.; Cai, N.S.; Huang, Y.Y.; Han, H.J. Synthesis, experimental studies, and analysis of a new calcium-based carbon dioxide absorbent. *Energy Fuels* **2005**, *19*, 1447–1452. [CrossRef]
28. Radfarnia, H.R.; Sayari, A. A highly efficient CaO-based CO_2 sorbent prepared by a citrate-assisted sol–gel technique. *Chem. Eng. J.* **2015**, *262*, 913–920. [CrossRef]
29. Broda, M.; Müller, C.R. Synthesis of Highly Efficient, Ca-Based, Al_2O_3-Stabilized, Carbon Gel-Templated CO_2 Sorbents. *Adv. Mater.* **2012**, *24*, 3059–3064. [CrossRef]
30. Li, Z.S.; Cai, N.S.; Huang, Y.Y. Effect of preparation temperature on cyclic CO_2 capture and multiple carbonation-calcination cycles for a new Ca-based CO_2 sorbent. *Ind. Eng. Chem. Res.* **2006**, *45*, 1911–1917. [CrossRef]
31. Barelli, L.; Bidini, G.; Di Michele, A.; Gallorini, F.; Petrillo, C.; Sacchetti, F. Synthesis and test of sorbents based on calcium aluminates for SE-SR. *Appl. Energy* **2014**, *127*, 81–92. [CrossRef]
32. Huang, L.; Zhang, Y.; Gao, W.; Harada, T.; Qin, Q.; Zheng, Q.; Hatton, T.A.; Wang, Q. Alkali Carbonate Molten Salt Coated Calcium Oxide with Highly Improved Carbon Dioxide Capture Capacity. *Energy Technol.* **2017**, *5*, 1328–1336. [CrossRef]
33. Takahashi, Y.; Sakamoto, R.; Kamimoto, M. Heat capacities and latent heats of $LiNO_3$, $NaNO_3$, and KNO_3. *Int. J. Thermophys.* **1988**, *9*, 1081–1090. [CrossRef]
34. Yang, Y.; Asta, M.; Laird, B.B. Solid-liquid interfacial premelting. *Phys. Rev. Lett.* **2013**, *110*, 096102. [CrossRef]
35. Albrecht, K.O.; Wagenbach, K.S.; Satrio, J.A.; Shanks, B.H.; Wheelock, T.D. Development of a CaO-based CO_2 sorbent with improved cyclic stability. *Ind. Eng. Chem. Res.* **2008**, *47*, 7841–7848. [CrossRef]
36. Hu, Y.; Lu, H.; Liu, W.; Yang, Y.; Li, H. Incorporation of CaO into inert supports for enhanced CO_2 capture: A review. *Chem. Eng. J.* **2020**, *396*, 125253. [CrossRef]
37. Li, L.; King, D.L.; Nie, Z.; Howard, C. Magnesia-stabilized calcium oxide absorbents with im-proved durability for high temperature CO_2 capture. *Ind. Eng. Chem. Res.* **2009**, *48*, 10604–10613. [CrossRef]
38. Guo, H.; Xu, Z.; Jiang, T.; Zhao, Y.; Ma, X.; Wang, S. The effect of incorporation Mg ions into the crystal lattice of CaO on the high temperature CO_2 capture. *J. CO2 Util.* **2020**, *37*, 335–345. [CrossRef]
39. Teixeira, P.; Fernandes, A.; Ribeiro, F.; Pinheiro, C.I.C. Blending wastes of marble powder and dolomite sorbents for calcium-looping CO_2 capture under realistic industrial calcination conditions. *Materials* **2021**, *14*, 4379. [CrossRef]
40. Valverde, J.M.; Sanchez-Jimenez, P.E.; Perez-Maqueda, L.A.; Quintanilla, M.A.S.; Perez-Vaquero, J. Role of crystal structure on CO_2 capture by limestone derived CaO subjected to carbona-tion/recarbonation/calcination cycles at Ca-looping conditions. *Appl. Energy* **2014**, *125*, 264–275. [CrossRef]
41. Sanchez-Jimenez, P.E.; Valverde, J.M.; Perez-Maqueda, L.A. Multicyclic conversion of limestone at Ca-looping conditions: The role of solid-sate diffusion controlled carbonation. *Fuel* **2014**, *127*, 131–140. [CrossRef]
42. Valverde, J.M.; Perejon, A.; Medina, S.; Perez-Maqueda, L.A. Thermal decomposition of dolomite under CO_2: Insights from TGA and in situ XRD analysis. *Phys. Chem. Chem. Phys.* **2015**, *17*, 30162–30176. [CrossRef] [PubMed]
43. Liu, B.; Thomas, P.S.; Ray, A.S.; Guerbois, J.P. A TG Analysis of the Effect of Calcination Condi-tions on the Properties of Reactive Magnesia. *J. Therm. Anal. Calorim.* **2007**, *88*, 145–149. [CrossRef]

44. Sun, J.; Liu, W.; Li, M.; Yang, X.; Wang, W.; Hu, Y.; Chen, H.; Li, X.; Xu, M. Mechanical Modification of Naturally Occurring Limestone for High-Temperature CO_2 Capture. *Energy Fuels* **2016**, *30*, 6597–6605. [CrossRef]
45. Song, G.; Zhu, X.; Chen, R.; Liao, Q.; Ding, Y.D.; Chen, L. Influence of the precursor on the porous structure and CO_2 adsorption characteristics of MgO. *RSC Adv.* **2016**, *6*, 19069–19077. [CrossRef]
46. Dunstan, M.T.; Donat, F.; Bork, A.H.; Grey, C.P.; Müller, C.R. CO_2 Capture at Medium to High Temperature Using Solid Oxide-Based Sorbents: Fundamental Aspects, Mechanistic Insights, and Recent Advances. *Chem. Rev.* **2021**, *121*, 12681–12745. [CrossRef]
47. Luo, T.; Liu, S.; Luo, C.; Qi, X.; Lu, B.; Zhang, L. Effect of different organic compounds on the preparation of CaO-based CO_2 sorbents derived from wet mixing combustion synthesis. *Chin. J. Chem. Eng.* **2021**, *36*, 157–169. [CrossRef]
48. Afandi, N.; Satgunam, M.; Mahalingam, S.; Manap, A.; Nagi, F.; Liu, W.; Johan, R.B.; Turan, A.; Tan, A.W.-Y.; Yunus, S. Review on the modifications of natural and industrial waste CaO based sorbent of calcium looping with enhanced CO_2 capture capacity. *Heliyon* **2024**, *10*, e24119. [CrossRef]
49. Rajamathi, R.; Bhojaraj; Nethravathi, C. Porous CaO-MgO Nanostructures for CO_2 Capture. *ACS Appl. Nano Mater.* **2021**, *4*, 10969–10975. [CrossRef]
50. Xu, Z.; Jiang, T.; Zhang, H.; Zhao, Y.; Ma, X.; Wang, S. Efficient MgO-doped CaO sorbent pellets for high temperature CO_2 capture. *Front. Chem. Sci. Eng.* **2021**, *15*, 698–708. [CrossRef]
51. Wang, K.; Gu, F.; Clough, P.T.; Zhao, P.; Anthony, E.J. Porous MgO-stabilized CaO-based pow-ders/pellets via a citric acid-based carbon template for thermochemical energy storage in con-centrated solar power plants. *Chem. Eng. J.* **2020**, *390*, 124163. [CrossRef]
52. Morales-Mendoza, J.E.; Jasso-Salcedo, A.B.; Domínguez-Arvizu, J.L.; Ibarra-Rodriguez, L.I.; Hernández-Majalca, B.C.; Bueno-Escobedo, J.L.; Salami, H.A.; Alalade, I.G.; Gaxiola-Cebreros, F.A.; Pérez-Hernández, L.; et al. CO_2 sorption and multicycle stability of dolomite promoted with Ba and Sr metals for sorption enhanced hydrogen production. *Int. J. Hydrogen Energy* 2025, *in press*. [CrossRef]
53. Herce, C.; Stendardo, S.; Cortés, C. Increasing CO_2 carrying capacity of dolomite by means of thermal stabilization by triggered calcination. *Chem. Eng. J.* **2015**, *262*, 18–28. [CrossRef]
54. Wardhani, S.; Prasetia, F.; Khunur, M.M.; Purwonugroho, D.; Prananto, Y.P. Effect of CO_2 Flow Rate and Carbonation Temperature in the Synthesis of Crystalline Precipitated Calcium Carbonate (PCC) from Limestone. *Indones. J. Chem.* **2018**, *18*, 573–579. [CrossRef]
55. Widiarti, N.; Holilah, H.; Bahruji, H.; Nugraha, R.E.; Suprapto, S.; Ni'mah, Y.L.; Prasetyoko, D. Coprecipitation and hydrothermal synthesis of CaO from dolomite in the presence of Sapindus rarak extract for biodiesel production: Catalysts characterization and optimization. *RSC Adv.* **2024**, *14*, 23332–23340. [CrossRef] [PubMed]
56. Koga, N.; Criado, J.M. The influence of mass transfer phenomena on the kinetic analysis for the thermal decomposition of calcium carbonate by constant rate thermal analysis (CRTA) under vacuum. *Int. J. Chem. Kinet.* **1998**, *30*, 737–744. [CrossRef]
57. Yang, X.; Zhao, L.; Yang, S.; Xiao, Y. Investigation of natural CaO-MgO sorbent for CO_2 capture. *Asia-Pac. J. Chem. Eng.* **2013**, *8*, 906–915. [CrossRef]
58. Li, X.; Xu, J.; Zhou, L.; Wang, F.; Gao, J.; Chen, C.; Ning, J.; Ma, H. Liquid-phase oxidation of toluene by molecular oxygen over copper manganese oxides. *Catal. Lett.* **2006**, *110*, 255–260. [CrossRef]
59. Goldsmith, J.R.; Graf, D.L. Structural and Compositional Variations in Some Natural Dolomites. *J. Geol.* **1958**, *66*, 678–693. [CrossRef]
60. Silaban, A.; Narcida, M.; Harrison, D.P. Characteristics of the reversible reaction between CO_2(g) and calcined dolomite. *Chem. Eng. Commun.* **1996**, *146*, 149–162. [CrossRef]
61. Yoosuk, B.; Udomsap, P.; Puttasawat, B. Hydration–dehydration technique for property and activity improvement of calcined natural dolomite in heterogeneous biodiesel production: Structural transformation aspect. *Appl. Catal. A Gen.* **2011**, *395*, 87–94. [CrossRef]
62. Resio, L.C. Dolomite thermal behaviour: A proposal to establish a definitive decomposition mechanism in a convective air atmosphere. *Open Ceram.* **2023**, *15*, 100405. [CrossRef]
63. Rodriguez-Navarro, C.; Kudlacz, K.; Ruiz-Agudo, E. The mechanism of thermal decomposition of dolomite: New insights from 2D-XRD and TEM analyses. *Am. Mineral.* **2012**, *97*, 38–51. [CrossRef]
64. Manovic, V.; Anthony, E.J. Thermal Activation of CaO-Based Sorbent and Self-Reactivation during CO_2 Capture Looping Cycles. *Environ. Sci. Technol.* **2008**, *42*, 4170–4174. [CrossRef] [PubMed]
65. German, R.M. *Thermodynamics of Sintering, Sintering of Advanced Materials*; Woodhead Publishing: Cambridge, UK, 2010; pp. 3–32. [CrossRef]
66. Thommes, M.; Kaneko, K.; Neimark, A.V.; Olivier, J.P.; Rodriguez-Reinoso, F.; Rouquerol, J.; Sing, K.S.W. Physisorption of gases, with special reference to the evaluation of surface area and pore size distribution (IUPAC Technical Report). *Pure Appl. Chem.* **2015**, *87*, 1051–1069. [CrossRef]

67. Gupta, H.; Fan, L.S. Carbonation-calcination cycle using high reactivity calcium oxide for carbon dioxide separation from flue gas. *Ind. Eng. Chem. Res.* **2002**, *41*, 4035–4042. [CrossRef]
68. Bindu, P.; Thomas, S. Estimation of lattice strain in ZnO nanoparticles: X-ray peak profile analysis. *J. Theor. Appl. Phys.* **2014**, *8*, 123–134. [CrossRef]
69. Motelica, L.; Oprea, O.C.; Vasile, B.S.; Ficai, A.; Ficai, D.; Andronescu, E.; Holban, A.M. Antibacterial Activity of Solvothermal Obtained ZnO Nanoparticles with Different Morphology and Photo-catalytic Activity against a Dye Mixture: Methylene Blue, Rhodamine B and Methyl Orange. *Int. J. Mol. Sci.* **2023**, *24*, 5677. [CrossRef]
70. Saleem, M. Effect of zinc acetate concentration on the structural and optical properties of ZnO thin films deposited by Sol-Gel method. *Int. J. Phys. Sci.* **2012**, *7*, 2971–2979. [CrossRef]
71. Alsaad, A.M.; Ahmad, A.A.; Al-Bataineh, Q.M.; Bani-Salameh, A.A.; Abdullah, H.S.; Qattan, I.A.; Albataineh, Z.M.; Telfah, A.D. Optical, Structural, and Crystal Defects Characterizations of Dip Synthesized (Fe-Ni) Co-Doped ZnO Thin Films. *Materials* **2020**, *13*, 1737. [CrossRef] [PubMed]
72. Zamora, D.A. Flash Calcined Magnesium Oxide Sorbents for CO_2 Adsorption and Catalytic Enhancement of the Water-Gas Shift Reaction. Ph.D. Thesis, UNSW Sydney, Kensington, Australia, 2021. [CrossRef]
73. Sánchez-Jiménez, P.E.; Valverde, J.M.; Perejón, A.; De La Calle, A.; Medina, S.; Pérez-Maqueda, L.A. Influence of Ball Milling on CaO Crystal Growth during Limestone and Dolomite Calcination: Effect on CO_2 Capture at Calcium Looping Conditions. *Cryst. Growth Des.* **2016**, *16*, 7025–7036. [CrossRef]
74. Busca, G.; Lorenzelli, V. Infrared spectroscopic identification of species arising from reactive adsorption of carbon oxides on metal oxide surfaces. *Mater. Chem.* **1982**, *7*, 89–126. [CrossRef]
75. Anderson, J.A.; Rochester, C.H. Infrared studies of probe molecules adsorbed on calcium oxide. *J. Chem. Soc. Faraday Trans. 1 Phys. Chem. Condens. Phases* **1986**, *82*, 1911–1922. [CrossRef]
76. Barros, M.C.; Bello, P.M.; Bao, M.; Torrado, J.J. From waste to commodity: Transforming shells into high purity calcium carbonate. *J. Clean. Prod.* **2009**, *17*, 400–407. [CrossRef]
77. Stanienda-Pilecki, K. *Effects of Dolomitization Processes in the Triassic Limestone of Tarnów Opolski Deposit*; Silesian University of Technology Press: Gliwice, Poland, 2011. Available online: https://www.researchgate.net/publication/261045819_Effects_of_dolomitization_processes_in_the_Triassic_limestone_of_Tarnow_Opolski_Deposit_Przejawy_dolomityzacji_w_wapieniach_triasowych_zloza_%E2%80%99Tarnow_Opolski%E2%80%99_Silesian_University_of_Technology_Press_Gl (accessed on 28 November 2024).
78. Stanienda-Pilecki, K. *Diagenesis of the Triassic Limestone from the Opole Silesia in the Aspect of Magnesian Calcite Presence*; Silesian University of Technology Press: Gliwice, Poland, 2013. Available online: https://www.researchgate.net/publication/261048993_Diagenesis_of_the_Triassic_limestone_from_the_Opole_Silesia_in_the_aspect_of_magnesian_calcite_presence_Diageneza_triasowych_wapieni_Slaska_Opolskiego_w_aspekcie_obecnosci_kalcytu_magnezowego (accessed on 28 November 2024).
79. Majchrzak-Kucęba, I.; Bukalak-Gaik, D. Regeneration performance of metal–organic frameworks: TG-Vacuum tests. *J. Therm. Anal. Calorim.* **2016**, *125*, 1461–1466. [CrossRef]
80. Zeng, H.; Qu, X.; Xu, D.; Luo, Y. Porous Adsorption Materials for Carbon Dioxide Capture in Industrial Flue Gas. *Front. Chem.* **2022**, *10*, 939701. [CrossRef]
81. De La Calle Martos, A.; Valverde, J.M.; Sanchez-Jimenez, P.E.; Perejón, A.; García-Garrido, C.; Perez-Maqueda, L.A. Effect of dolomite decomposition under CO_2 on its multicycle CO_2 capture behaviour under calcium looping conditions. *Phys. Chem. Chem. Phys.* **2016**, *18*, 16325–16336. [CrossRef] [PubMed]
82. Valverde, J.M.; Sanchez-Jimenez, P.E.; Perez-Maqueda, L.A. Ca-looping for postcombustion CO_2 capture: A comparative analysis on the performances of dolomite and limestone. *Appl. Energy* **2015**, *138*, 202–215. [CrossRef]
83. Naeem, M.A.; Armutlulu, A.; Imtiaz, Q.; Donat, F.; Schäublin, R.; Kierzkowska, A.; Müller, C.R. Optimization of the structural characteristics of CaO and its effective stabilization yield high-capacity CO_2 sorbents. *Nat. Commun.* **2018**, *9*, 2408. [CrossRef]
84. Luo, C.; Zheng, Y.; Wu, Q.-L.; Ding, N.; Zheng, C.-G. Cyclic reaction characters of novel CaO/MgO high temperature CO_2 sorbents. *J. Eng. Thermophys.* **2011**, *32*, 1957–1960.
85. Hassanzadeh, A.; Abbasian, J. Regenerable MgO-based sorbents for high-temperature CO_2 removal from syngas: 1. Sorbent development, evaluation, and reaction modeling. *Fuel* **2010**, *89*, 1287–1297. [CrossRef]
86. Duan, Y.; Luebke, D.; Pennline, H.H.; Duan, Y.; Luebke, D.; Pennline, H.H. Efficient Theoretical Screening of Solid Sorbents for CO_2 Capture Applications. *Int. J. Clean Coal Energy* **2012**, *1*, 1–11. [CrossRef]
87. Dolabella, S.; Borzì, A.; Dommann, A.; Neels, A. Lattice Strain and Defects Analysis in Nanostructured Semiconductor Materials and Devices by High-Resolution X-Ray Diffraction: Theoretical and Practical Aspects. *Small Methods* **2022**, *6*, 2100932. [CrossRef]
88. Ishikawa, K.; Fujima, N.; Komura, H. First-order Raman scattering in MgO microcrystals. *J. Appl. Phys.* **1985**, *57*, 973–975. [CrossRef]
89. Galvan-Ruiz, M.; Baños, L.; Rodriguez-Garcia, M.E. Lime characterization as a food additive. *Sens. Instrumen. Food Qual.* **2007**, *1*, 169–175. [CrossRef]

90. Schmid, T.; Dariz, P. Shedding light onto the spectra of lime: Raman and luminescence bands of CaO, $Ca(OH)_2$ and $CaCO_3$. *J. Raman Spectrosc.* **2015**, *46*, 141–146. [CrossRef]
91. Dekermenjian, M.; Ruediger, A.P.; Merlen, A. Raman spectroscopy inves-tigation of magnesium oxide nanoparticles. *RSC Adv.* **2023**, *13*, 26683–26689. [CrossRef]
92. El-Sayed, E.M.; Hamad, H.A.; Ali, R.M. Journey from ceramic waste to highly efficient toxic dye adsorption from aqueous solutions via one-pot synthesis of $CaSO_4$ rod-shape with silica. *J. Mater. Res. Technol.* **2020**, *9*, 16051–16063. [CrossRef]
93. Campbell, I.H.; Fauchet, P.M. The effects of microcrystal size and shape on the one phonon Raman spectra of crystalline semiconductors. *Solid State Commun.* **1986**, *58*, 739–741. [CrossRef]
94. Parker, J.C.; Siegel, R.W. Calibration of the Raman spectrum to the oxygen stoichiometry of nanophase TiO_2. *Appl. Phys. Lett.* **1990**, *57*, 943. [CrossRef]
95. Wellner, A.; Paillard, V.; Bonafos, C.; Coffin, H.; Claverie, A.; Schmidt, B.; Heinig, K.H. Stress measurements of germanium nanocrystals embedded in silicon oxide. *J. Appl. Phys.* **2003**, *94*, 5639–5642. [CrossRef]
96. Hoogewijs, R.; Fiermans, L.; Vennik, J. Electronic relaxation processes in the KLL′ auger spectra of the free magnesium atom, solid magnesium and MgO. *J. Electron Spectrosc. Relat. Phenom.* **1977**, *11*, 171–183. [CrossRef]
97. Wang, J.; Mueller, D.N.; Crumlin, E.J. Recommended strategies for quantifying oxygen vacancies with X-ray photoelectron spectroscopy. *J. Eur. Ceram. Soc.* **2024**, *44*, 116709. [CrossRef]
98. Zhang, C.; Wang, C.; Zhan, W.; Guo, Y.; Guo, Y.; Lu, G.; Baylet, A.; Giroir-Fendler, A. Catalytic oxi-dation of vinyl chloride emission over $LaMnO_3$ and $LaB_{0.2}Mn_{0.8}O_3$ (B = Co, Ni, Fe) catalysts. *Appl. Catal. B* **2013**, *129*, 509–516. [CrossRef]
99. Yan, X.; Li, Y.; Sun, C.; Zhang, C.; Yang, L.; Fan, X.; Chu, L. Enhanced H_2 production from steam gasification of biomass by red mud-doped Ca-Al-Ce bi-functional material. *Appl. Energy* **2022**, *312*, 118737. [CrossRef]
100. Zhang, C.; Li, Y.; He, Z.; Zhao, J.; Wang, D. Microtubular Fe/Mn-promoted CaO-$Ca_{12}Al_{14}O_{33}$ bi-functional material for H_2 production from sorption enhanced water gas shift. *Appl. Catal. B* **2022**, *314*, 121474. [CrossRef]
101. Henderson, M.A. A surface science perspective on TiO_2 photocatalysis. *Surf. Sci. Rep.* **2011**, *66*, 185–297. [CrossRef]
102. Thompson, T.L.; Diwald, O.; Yates, J.T. CO_2 as a probe for monitoring the surface defects on TiO_2(110)-temperature-programmed desorption. *J. Phys. Chem. B* **2003**, *107*, 11700–11704. [CrossRef]
103. Rawool, S.A.; Yadav, K.K.; Polshettiwar, V. Defective TiO_2 for photocatalytic CO_2 conversion to fuels and chemicals. *Chem. Sci.* **2021**, *12*, 4267. [CrossRef]
104. Zhu, C.; Huang, H.; Hu, H.; Fang, J.; Mao, J. Modulation of oxygen vacancies and hot electrons promotes highly efficient CO_2 photoreduction towards C_2H_6. *Nano Res.* **2025**, *18*, 94907275. [CrossRef]
105. Wang, Y.; Memon, M.Z.; Xie, Q.; Gao, Y.; Li, A.; Fu, W.; Wu, Z.; Dong, Y.; Ji, G. Study on CO_2 sorption performance and sorption kinetics of Ce- and Zr-doped CaO-based sorbents. *Carbon Capture Sci. Technol.* **2022**, *2*, 100033. [CrossRef]
106. Lee, C.H.; Choi, S.W.; Yoon, H.J.; Kwon, H.J.; Lee, H.C.; Jeon, S.G.; Lee, K.B. Na_2CO_3-doped CaO-based high-temperature CO_2 sorbent and its sorption kinetics. *Chem. Eng. J.* **2018**, *352*, 103–109. [CrossRef]
107. Zheng, Y.; Ge, Z.; Sun, H.; Wang, L.; Zhang, S.; Lin, X.; Chen, Q.; Chen, H. The role of oxygen vacancy in CaO-$Ca_{12}Al_{14}O_{33}$ materials derived from hydrocalumite for enhanced CO_2 capture cyclic performance. *Chem. Eng. J.* **2024**, *481*, 147955. [CrossRef]
108. Pacchioni, G. Physisorbed and chemisorbed CO_2 at surface and step sites of the MgO (100) surface. *Surf. Sci.* **1993**, *281*, 207–219. [CrossRef]
109. Jensen, M.B.; Pettersson, L.G.M.; Swang, O.; Olsbye, U. CO_2 sorption on MgO and CaO surfaces: A comparative quantum chemical cluster study. *J. Phys. Chem. B* **2005**, *109*, 16774–16781. [CrossRef] [PubMed]
110. Du, H.; Williams, C.T.; Ebner, A.D.; Ritter, J.A. In situ FTIR spectroscopic analysis of carbonate transformations during adsorption and desorption of CO_2 in K-promoted HTlc. *Chem. Mater.* **2010**, *22*, 3519–3526. [CrossRef]
111. Li, X.; An, M.; Zhu, Y.; Ma, H. First-principles study adsorption properties of CO_2 molecule on CaO(100) surfaces. In Proceedings of the 2015 2nd International Workshop on Materials Engineering and Computer Sciences, Jinan, China, 10–11 October 2015. [CrossRef]
112. Liu, L.; Hong, D.; Feng, Y.; Guo, X. Promoted CaO-Based CO_2 Sorbents by First-Principles Cal-Culations. *Ranshao Kexue Yu Jishu/J. Combust. Sci. Technol.* **2017**, *23*, 412–417.
113. Solis, B.H.; Cui, Y.; Weng, X.; Seifert, J.; Schauermann, S.; Sauer, J.; Shaikhutdinov, S.; Freund, H.-J. Initial stages of CO_2 adsorption on CaO: A combined experimental and computational study. *Phys. Chem. Chem. Phys.* **2017**, *19*, 4231–4242. [CrossRef]
114. Yan, X.; Duan, C.; Yu, S.; Dai, B.; Sun, C.; Chu, H. Revealing the mechanism of oxygen vacancy defect for CO_2 adsorption and diffusion on CaO: DFT and experimental study. *J. CO2 Util.* **2024**, *79*, 102648. [CrossRef]
115. Krödel, M.; Landuyt, A.; Abdala, P.M.; Müller, C.R. Mechanistic Understanding of CaO-Based Sorbents for High-Temperature CO_2 Capture: Advanced Characterization and Prospects. *ChemSusChem* **2020**, *13*, 6259–6272. [CrossRef]
116. Hu, J.; Jiang, Y.; Gao, Q.; Zhao, Y.; Dai, S.; Li, X.; Wei, W. Material engineering of porous calcium oxide for boosting CO_2 capture. *Chem. Eng. J.* **2025**, *505*, 159237. [CrossRef]

117. Miranda-Pizarro, J.; Perejón, A.; Valverde, J.M.; Pérez-Maqueda, L.A.; Sánchez-Jiménez, P.E. CO_2 capture performance of Ca-Mg acetates at realistic Calcium Looping conditions. *Fuel* **2017**, *196*, 497–507. [CrossRef]
118. Wang, K.; Yin, Z.; Zhao, P.; Han, D.; Hu, X.; Zhang, G. Effect of Chemical and Physical Treatments on the Properties of a Dolomite Used in Ca Looping. *Energy Fuels* **2015**, *29*, 4428–4435. [CrossRef]
119. Wang, K.; Hu, X.; Zhao, P.; Yin, Z. Natural dolomite modified with carbon coating for cyclic high-temperature CO_2 capture. *Appl. Energy* **2016**, *165*, 14–21. [CrossRef]
120. Wang, K.; Gu, F.; Clough, P.T.; Zhao, P.; Anthony, E.J. CO_2 Capture Performance of Gluconic Acid Modified Limestone-Dolomite Mixtures under Realistic Conditions. *Energy Fuels* **2019**, *33*, 7550–7560. [CrossRef]
121. Han, R.; Xing, S.; Wu, X.; Pang, C.; Lu, S.; Su, Y.; Liu, Q.; Song, C.; Gao, J. Relevant influence of alkali carbonate doping on the thermochemical energy storage of Ca-based natural minerals during $CaO/CaCO_3$ cycles. *Renew. Energy* **2022**, *181*, 267–277. [CrossRef]
122. Srinivasan, S.; Dodson, D.; Charles, M.B.J.; Wallen, S.L.; Albarelli, G.; Kaushik, A.; Hickman, N.; Chaudhary, G.R.; Stefanakos, E.; Dhau, J. Energy storage in earth-abundant dolomite minerals. *Appl. Sci.* **2020**, *10*, 6679. [CrossRef]
123. Wang, F.; Kuzuya, T.; Hirai, S.; Li, J.; Li, T. Carbon dioxide absorption and release properties of pyrolysis products of dolomite calcined in vacuum atmosphere. *Sci. World J.* **2014**, *2014*, 862762. [CrossRef]
124. Hildenbrand, N.; Readman, J.; Dahl, I.M.; Blom, R. Sorbent enhanced steam reforming (SESR) of methane using dolomite as internal carbon dioxide absorbent: Limitations due to $Ca(OH)_2$ formation. *Appl. Catal. A Gen.* **2006**, *303*, 131–137. [CrossRef]
125. Oliveira, C.C.; Hori, C.E. Hydrogen production from sorption enhanced steam reforming of ethanol using bifunctional Ni and Ca-based catalysts doped with Mg and Al. *Int. J. Hydrogen Energy* **2023**, *48*, 30263–30281. [CrossRef]
126. Zeng, P.; Dou, B.; Zhang, H.; Wu, K.; Zhao, L.; Luo, C.; Chen, H.; Xu, Y. Chemical looping steam reforming of ethanol without and with in-situ CO_2 capture. *Int. J. Hydrogen Energy* **2022**, *47*, 6552–6568. [CrossRef]

Disclaimer/Publisher's Note: The statements, opinions and data contained in all publications are solely those of the individual author(s) and contributor(s) and not of MDPI and/or the editor(s). MDPI and/or the editor(s) disclaim responsibility for any injury to people or property resulting from any ideas, methods, instructions or products referred to in the content.